Available online at www.sciencedirect.com
SCIENCE DIRECT®
ELSEVIER
European Journal of Mechanics B/Fluids 22 (2003) 555–579
EUROPEAN JOURNAL OF MECHANICS B/FLUIDS

A new Finite Element Method for magneto-dynamical problems: two-dimensional results

J.L. Guermond [a,1], J. Léorat [b], C. Nore [a,*,2]

[a] *Laboratoire d'informatique pour la mécanique et les sciences de l'ingénieur, CNRS, BP 133, 91403 Orsay cedex, France*
[b] *Luth, Observatoire de Paris-Meudon, place Janssen, 92195 Meudon, France*

Received 26 February 2003; received in revised form 17 June 2003; accepted 17 June 2003

Abstract

A mixed Lagrange finite element technique is used to solve the Maxwell equations in the magneto-hydrodynamic (MHD) limit in an hybrid domain composed of vacuum and conducting regions. The originality of the approach is that no artificial boundary condition is enforced at the interface between the conducting and the insulating regions and the non-conducting medium is not approximated by a weakly conducting medium as is frequently done in the literature. As a first evaluation of the performance of the method, we study two-dimensional (2D) configurations, where the flow streamlines of the conducting fluid are planar, i.e., invariant in one direction, and either the magnetic field ("magnetic scalar" case) or the electric field ("electric scalar" case) is parallel to the invariant direction. Induction heating, eddy current generation, and magnetic field stretching are investigated showing the usefulness of finite element methods to solve magneto-dynamical problems with complex insulating boundaries.

Keywords: Finite element method; 2D magnetodynamics

1. Introduction

1.1. Introductory comments

Magneto-hydrodynamic (MHD) flows are usually involved in two well separated contexts: industrial applications (e.g., metallurgy, electromechanics) and astrophysical problems. The difference stems from the magnitude of the magnetic Reynolds number, R_m, which compares the magnetic diffusion typical time to the advection characteristic time. In industrial applications, R_m is well below unity so that the induced magnetic fields may be neglected, while, in astrophysics, R_m is much larger than unity and conversion of kinetic energy into magnetic energy through the so-called dynamo action takes place. We refer to Moffatt [1] for a survey on the physical aspects of the dynamo action.

The equations that model the dynamo action are the incompressible Navier–Stokes equations and the Maxwell equations with the displacement-currents neglected, the two sets of equations being coupled via the Lorentz force and the Ohm's law.

The Maxwell equations involve four vector fields, **E**, **H**, **D**, and **B**, the electric field, the magnetic field, the electric induction, and the magnetic induction, respectively. These four vector fields are related by two constitutive equations depending on the polarization properties of the material. Henceforth we assume linearity: the magnetic permeability $\mu = \mu(\mathbf{x})$, the electric

* Corresponding author.
E-mail address: nore@limsi.fr (C. Nore).
[1] Present address: TICAM, The University of Texas at Austin, TX 78712, USA.
[2] Université Paris XI, Département de Physique, 91405 Orsay cedex, France.

0997-7546/$ – see front matter
doi:10.1016/S0997-7546(03)00054-2

permittivity $\varepsilon = \varepsilon(\mathbf{x})$, and the conductivity $\sigma = \sigma(\mathbf{x})$ are positive functions of the space position $\mathbf{x}$ but do not depend on the electromagnetic field. Then, the electromagnetic field can be represented by two vector fields only: the electric field $\mathbf{E}$ and the magnetic field $\mathbf{H}$.

The conducting fluid is assumed to be of unit density and the flow to be incompressible. We denote by $\mathbf{u}$ the velocity, p the pressure and ν the kinematic viscosity.

Being given source terms, $\mathbf{f}$, $\mathbf{j}$, and initial data, $\mathbf{u}_0$, and $\mathbf{H}_0$, the set of equations is as follows:

$$\begin{cases} \partial_t \mathbf{u} + (\mathbf{u}\cdot\nabla)\mathbf{u} - \nu\Delta\mathbf{u} + \nabla p = (\nabla\times\mathbf{H})\times\mu\mathbf{H} + \mathbf{f} & \text{in } \Omega_c, \\ \nabla\cdot\mathbf{u} = 0 & \text{in } \Omega_c, \\ \mathbf{u}|_{\partial\Omega_c} = 0, \\ \mathbf{u}|_{t=0} = \mathbf{u}_0, \end{cases} \tag{1}$$

$$\begin{cases} \partial_t(\mu\mathbf{H}) = -\nabla\times\mathbf{E} & \text{in } \Omega, \\ \nabla\times\mathbf{H} = \sigma\big(\mathbf{E} + \mathbf{u}\times(\mu\mathbf{H})\big) + \mathbf{j}_s & \text{in } \Omega_c, \\ \nabla\times\mathbf{H} = 0 & \text{in } \Omega_v, \\ \nabla\cdot(\varepsilon\mathbf{E}) = 0 & \text{in } \Omega_v, \\ \mathbf{H}\times\mathbf{n}|_{\Gamma} = 0, \\ \mathbf{E}\cdot\mathbf{n}|_{\Gamma_v} = 0, \\ \mathbf{H}|_{t=0} = \mathbf{H}_0, \end{cases} \tag{2}$$

where Ω_c denotes the domain occupied by the conducting fluid, Ω_v is the domain of the non-conducting medium, and $\Omega = \Omega_c \cup \Omega_v$ is the total domain. The subscripts c and v stand for conductor and vacuum respectively. To refer to boundary conditions easily, we introduce

$$\Gamma_c = \partial\Omega \cap \partial\Omega_c, \quad \Gamma_v = \partial\Omega \cap \partial\Omega_v, \quad \Sigma = \partial\Omega_c \cap \partial\Omega_v, \quad \Gamma = \partial\Omega = \Gamma_v \cup \Gamma_c. \tag{3}$$

Γ is the boundary of Ω, $\mathbf{n}$ the outward normal to Γ, Σ the interface between Ω_c and Ω_v. Three possible partitions of Ω considered henceforth are shown on Fig. 1.

The boundary data are taken homogeneous for the sake of simplicity, but general inhomogeneous data can be accounted for in the present framework by using appropriate liftings of the boundary data.

Although a coupled set of Partial Differential Equations is to be solved, the main numerical difficulty encountered in the astrophysical context does not come from the coupling but from the presence of the non-conducting medium where the conductivity is zero. In this region the magnetic field $\mathbf{H}$ must be curl-free (it derives from a scalar potential) and the electric induction divergence-free (it derives from a vector potential). If it were not for this condition (in other words, if $\Omega = \Omega_c$), then the electric field could be eliminated from the system of equations as is done in most industrial applications and the resulting equations would be parabolic, thus posing no particular difficulty to be approximated numerically (see, e.g., [2–4]).

Most of the existing numerical works dedicated to the dynamo problem either assume that the conducting region has perfectly conducting walls ("ideal" boundary), or enforce an *ad hoc* boundary condition on $\mathbf{H}$ at the interface Σ, so that the problem can be restricted to the conducting region only. Few studies consider the MHD equations with "non-ideal" boundaries and most of them are either restricted to steady situations (see, for example, [5] and the references therein), or consider simple geometries for the conducting region, like infinite cylinders or spheres, so that the exterior problem can be solved analytically [6–8]. In the stationary case with "non-ideal" boundary, the magnetic field is usually eliminated by means of the Biot–Savart law as suggested in [5].

Industrial applications, usually characterized by $R_m \ll 1$, generally involve complex boundaries. This has led to the brisk development of Finite Element codes in this field. In astrophysical situations with $R_m \gg 1$, the boundaries generally have a much simpler geometry than in the industrial cases, i.e., spherical symmetry or periodicity, so that the treatment of the magnetic boundary/interface conditions remains analytically and numerically tractable. However, this trend is now changing. Recently, two experimental demonstrations of the dynamo effect have been performed in cylindrical containers using sodium flows [9,10]

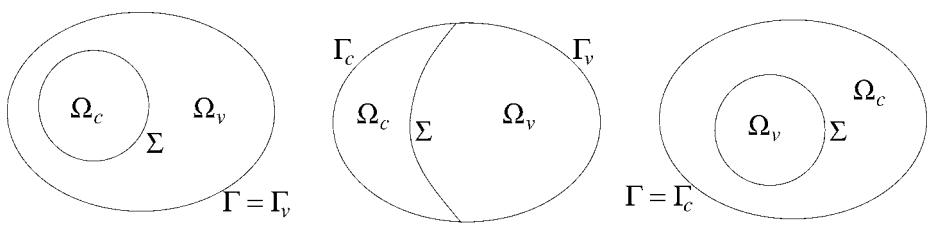

Fig. 1. Three possible settings for the domain.

at magnetic Reynolds numbers close to 60. Related computations have correctly predicted dynamo thresholds [11,12] using approximations of both the geometry and the experimental boundary conditions, and based on a schematic representation of the flow field. Another experimental set-up at similar magnetic Reynolds numbers is currently operated in a turbulent swirling flow of liquid sodium [13]. Numerical computations based on axially periodic flow have predicted the dynamo threshold at $R_m \approx 70$ [14], which is not reached in the present facility. The optimization of experiments of this type requires a proper treatment of the boundary conditions and a better account of the non-conducting medium surrounding the containers. This is one of the physical motivations of the present work.

Although the Finite Element Method (FEM) has proven its ability to solve the hydrodynamic equations in a large variety of industrial configurations, it is only recently that it has been considered for solving the dynamo problem. For instance, finite elements have been applied to the spherical dynamo problem by Chan et al. [15]. However, like most of the early attempts at solving the dynamo problem by using FEM, the method used in [15] is not completely satisfactory, since the insulating region is modeled by a weakly conducting one. The aim of the present paper is to solve dynamo-like problems by accounting exactly for the insulating region without any sort of penalization.

1.2. Goals of the paper

In the present paper, we intend to use a recently proposed algorithm designed for solving confined MHD flows at large magnetic Reynolds numbers. The mathematical properties of the algorithm in question have been analyzed in detail in [16] in 2D and in [17] in 3D. Our objective is to assess the performance of this new algorithm and to apply it effectively to some physically relevant 2D flows, including the few for which analytical results are available, postponing all 3D applications (including dynamo action) to a further work.

The outline of the paper is as follows. We introduce the electric scalar and the magnetic scalar formulations in Section 2. We also give in this section details for building the corresponding finite element approximations. In Section 3, we study the electric scalar case. Three configurations are investigated. We first evaluate the Ohmic decay in a circular cylinder. Then we analyze the time evolution of the patterns made by the magnetic lines in the case of impulsively started solid rotors embedded either in insulating or conducting media. We finally study the shearing effects of eddies on the magnetic field. In Section 4, we study the magnetic scalar case. We consider four test cases: Ohmic decay; forced heating; eddy currents induced by magnetic braking; currents flowing in a compound domain. In each case, numerical results are compared to analytic solutions when available. Concluding remarks are reported in Section 5.

1.3. Notations

We denote the Cartesian coordinates in $\mathbb{R}^3$ by (x, y, z) and the cylindrical coordinates by (r, φ, z). In the numerical simulations presented hereafter we assume that z is an invariant direction. We assume also that the velocity of the field flow, $\mathbf{u}$, is known and is everywhere normal to the invariant direction z, i.e., $\mathbf{u} = (u_x(x, y, t), u_y(x, y, t), 0)$. Using the Maxwell equations, the boundary conditions, and the initial data, it can be inferred that two classes of 2D solutions exist. Either $\mathbf{H} = (0, 0, H)$ and $E_z = 0$, or $\mathbf{E} = (0, 0, E)$ and $H_z = 0$. The first case is henceforth referred to as the magnetic scalar situation, whereas the second case is referred to as the electric scalar configuration. In the first case $\mathbf{H}$ is a scalar and $\nabla\cdot(\mu\mathbf{H}) = 0$ is automatically fulfilled. In the second case $\mathbf{E}$ is scalar and $\nabla\cdot(\varepsilon\mathbf{E}) = 0$ is fulfilled trivially. These particular 2D cases may appear too restricted and academic with respect to the nonlinear dynamo problem. Nonetheless, they are related to interesting physical situations, and they lead to nontrivial numerical problems. The algorithms for solving these problems are reduced versions of those required for the more general 3D formulation, thus their study is a prerequisite for the forthcoming unrestricted 3D case.

In all the numerical tests reported in Sections 3 and 4, we assume $\varepsilon = \mu = \sigma = 1$.

2. The Finite Element Method (FEM) algorithm

In this section we introduce the electric scalar and magnetic scalar formulations together with their respective finite element approximation. Some details on the full 3D problem are also given.

2.1. 2D Electric scalar formulation

We start by describing the 2D Electric scalar formulation. In this situation, the set of Eqs. (2) simplifies as follows

$$\begin{cases} \partial_t(\mu\mathbf{H}) = -\nabla\times E & \text{in } \Omega, \\ \nabla\times\mathbf{H} = \sigma(E + \mathbf{u}\times(\mu\mathbf{H})) + j & \text{in } \Omega_c, \\ \nabla\times\mathbf{H} = 0 & \text{in } \Omega_v, \\ \mathbf{H}\times\mathbf{n} = 0 & \text{on } \Gamma, \\ \mathbf{H} = \mathbf{H}_0 & \text{at } t = 0, \end{cases} \tag{4}$$

where we adopt the following notations:

$$\nabla\times\mathbf{H} = \partial_x H_y - \partial_y H_x, \qquad \nabla\times E = (\partial_y E, -\partial_x E), \qquad \mathbf{u}\times(\mu\mathbf{H}) = \mu(u_x H_y - u_y H_x). \tag{5}$$

2.1.1. Stabilized weak formulation

To obtain a weak form of the system (4), we multiply the first equation by test functions and we integrate over Ω:

$$\nabla\times\mathbf{H} = (0, 0, \partial_x H_y - \partial_y H_x), \qquad \nabla\times E = (\partial_y E, -\partial_x E, 0), \qquad \mathbf{u}\times(\mu\mathbf{H}) = \big(0, 0, \mu(u_x H_y - u_y H_x)\big), \tag{6}$$

where $\mathbf{b}$ are the test functions to be chosen later and $(\cdot,\cdot)_\Omega$ denotes the L^2-scalar product on Ω. Now we integrate by parts the second term in the equation and, by restricting the test functions $\mathbf{b}$ to satisfy the same essential boundary condition as $\mathbf{H}$, i.e., $\mathbf{b}\times\mathbf{n}|_\Gamma = 0$, we obtain

$$(\mu\partial_t\mathbf{H}, \mathbf{b})_\Omega + (E, \nabla\times\mathbf{b})_\Omega = 0, \quad \forall\mathbf{b} \text{ s.t. } \mathbf{b}\times\mathbf{n}|_\Gamma = 0. \tag{7}$$

The second integral in this equation can be represented as a sum of integrals over Ω_c and Ω_v. Then taking into account that in the conducting medium Ω_c we have

$$E = \frac{1}{\sigma}(\nabla\times\mathbf{H} - j) - \mathbf{u}\times(\mu\mathbf{H}), \tag{8}$$

we obtain

$$(\mu\partial_t\mathbf{H}, \mathbf{b})_\Omega + \left(\frac{1}{\sigma}\nabla\times\mathbf{H}, \nabla\times\mathbf{b}\right)_{\Omega_c} - (\mathbf{u}\times\mu\mathbf{H}, \nabla\times\mathbf{b})_{\Omega_c} + (E, \nabla\times\mathbf{b})_{\Omega_v} = \left(\frac{1}{\sigma}j, \nabla\times\mathbf{b}\right)_{\Omega_c}, \quad \forall\mathbf{b}. \tag{9}$$

Although it can be shown that this form of Ampère's theorem yields a well posed problem, we can freely guarantee some additional control on the curl of $\mathbf{H}$ in the insulating region by adding the quantity $(\nabla\times\mathbf{H}, \nabla\times\mathbf{b})_{\Omega_v}$ to the above bilinear form.

At this point we want to emphasize also that, contrary to what is sometimes claimed by some authors, the equation $\nabla\cdot(\mu\mathbf{H}) = 0$ is not part of the original system (4). In other words, the constraint $\nabla\cdot(\mu\mathbf{H}) = 0$ need not be enforced for (4) to be well posed. This equation is just an *a posteriori* consequence of (4) provided the initial data also satisfy this equation. Nevertheless, it is standard to incorporate this equation in stabilized formulations to have an *a priori* control on the divergence of $\mu\mathbf{H}$. For instance we refer to [18] or [4] where this type of stabilization is used in conjunction with standard Lagrange finite elements to solve MHD problems in conducting media with constant properties. Hence we can freely add the quantity $(\nabla\cdot\mu\mathbf{H}, \nabla\cdot\mu\mathbf{b})_\Omega$ to the weak form of Ampère's theorem and still be guaranteed to solve the correct problem.

Let us define $\tilde\sigma$ to be a smooth extension of σ on the whole domain Ω so that for all $\mathbf{x}\in\Omega$, $\inf_{\mathbf{y}\in\Omega_c}\sigma(\mathbf{y}) \leqslant \tilde\sigma(\mathbf{x}) \leqslant \sup_{\mathbf{y}\in\Omega_c}\sigma(\mathbf{y})$. We now define the following stabilized bilinear form

$$a_s(\mathbf{H}, \mathbf{b}) = \left(\frac{1}{\tilde\sigma}\nabla\times\mathbf{H}, \nabla\times\mathbf{b}\right)_\Omega + \big(\nabla\cdot(\mu\mathbf{H}), \nabla\cdot(\mu\mathbf{b})\big)_\Omega - \big(\mathbf{u}\times(\mu\mathbf{H}), \nabla\times\mathbf{b}\big)_{\Omega_c}. \tag{10}$$

Now, we weakly enforce the constraint $\nabla\times\mathbf{H} = 0$ in Ω_v as follows

$$(\nabla\times\mathbf{H}, e)_{\Omega_v} = 0 \quad \forall e. \tag{11}$$

Finally we consider the following problem: for j given and $\mathbf{H}_0$ such that $\nabla\cdot(\mu\mathbf{H}_0) = 0$,

$$\begin{cases} \text{Find } \mathbf{H} \text{ with } \mathbf{H}\times\mathbf{n}|_\Gamma = 0 \text{ and } E \text{ s.t.,} \\ \mathbf{H}|_{t=0} = \mathbf{H}_0, \\ (\mu\partial_t\mathbf{H}, \mathbf{b})_\Omega + a_s(\mathbf{H}, \mathbf{b}) + (E, \nabla\times\mathbf{b})_{\Omega_v} = \left(\frac{1}{\sigma}j, \nabla\times\mathbf{b}\right)_{\Omega_c}, \quad \forall\mathbf{b} \text{ with } \mathbf{b}\times\mathbf{n}|_\Gamma = 0, \\ (\nabla\times\mathbf{H}, e)_{\Omega_v} = 0, \quad \forall e. \end{cases} \tag{12}$$

This problem is shown to be well posed and equivalent to the original problem (4) in [16].

At this point it is worth noting that the presence of the insulating region gives to the problem a saddle point structure where the electric field in the insulating region is the Lagrange multiplier that enforces the magnetic field to be curl-free. It seems that this structure, which is partly responsible for the numerical difficulties referred to in the introduction for solving the MHD equations with insulating regions, has been recognized only recently [16].

2.1.2. Finite element discretization

In this section we consider the finite element discretization of the formulation considered above. We shall denote by $(\mathcal{T}_h)_{h>0}$ a family of regular meshes covering Ω and composed of triangles.

We introduce $\mathbf{X}_h$ the space of the vector-valued continuous finite element functions which are piecewise quadratic on each triangle of the mesh and satisfy $\mathbf{b}_h \times \mathbf{n}|_\Gamma = 0$. We denote by M_h the space of the scalar-valued continuous finite element functions which are piecewise linear.

Denoting by $\mathcal{I}_h$ the Lagrange interpolation operator and by d_t the finite difference temporal operator, we build an approximate solution to (12) as follows:

$$\begin{cases} \text{Find } \mathbf{H}_h \in \mathcal{C}^1(0,T;\mathbf{X}_h) \text{ and } E_h \in \mathcal{C}^0(0,T;M_h) \text{ s.t.,} \\ (\mu d_t \mathbf{H}_h, \mathbf{b}_h)_\Omega + a_s(\mathbf{H}_h,\mathbf{b}_h) + (E_h, \nabla\times\mathbf{b}_h)_{\Omega_v} = \left(\dfrac{1}{\sigma} j, \nabla\times\mathbf{b}_h\right)_{\Omega_c}, \quad \forall \mathbf{b}_h \in \mathbf{X}_h, \\ (\nabla\times\mathbf{H}_h, e_h)_{\Omega_v} = 0, \quad \forall e_h \in M_h, \\ \mathbf{H}_h|_{t=0} = \mathcal{I}_h \mathbf{H}_0. \end{cases} \tag{13}$$

The saddle point structure of the problem is our main reason for choosing two different types of interpolation for the magnetic and the electric fields. In fact the problem is well posed if and only if there is a constant $\beta > 0$ such that

$$\forall e_h \in M_h, \quad \sup_{\mathbf{b}_h \in \mathbf{X}_h} \frac{(\nabla\times\mathbf{b}_h, e_h)_{\Omega_v}}{\|\mathbf{b}_h\|_{\mathbf{X}}} \geqslant \beta \|e_h\|_M, \tag{14}$$

where we have defined the norms

$$\|\mathbf{b}\|_{\mathbf{X}}^2 = \int_\Omega \left(\mathbf{b}^2 + (\nabla\times\mathbf{b})^2\right) \mathrm{d}\mathbf{x}, \qquad \|e\|_M^2 = \int_\Omega e^2 \,\mathrm{d}\mathbf{x}. \tag{15}$$

It is shown in [16] that using piecewise quadratic polynomials for the magnetic field and piecewise linear polynomials for the electric field guarantees that the above so-called inf-sup condition is satisfied with β independent of the mesh size.

In the numerical tests reported in this paper, the time derivative is approximated by means of the second order Backward Difference Formula (BDF2).

2.2. Magnetic scalar formulation and 3D formulation

Although in the numerical applications we shall restrict ourselves to the 2D magnetic scalar formulation, we present now the complete 3D theory, since the 2D magnetic scalar formulation and the full 3D theory are almost identical.

2.2.1. Stabilized weak formulation

We now consider the initial-boundary-value problem (2). Note that the equations $\nabla\times\mathbf{H}|_{\Omega_v} = 0$, $\nabla\cdot\varepsilon\mathbf{E}|_{\Omega_v} = 0$, and $\mathbf{E}\cdot\mathbf{n}|_{\Gamma_v} = 0$ are the trace of Ampère's theorem $\mu\varepsilon\partial_t\mathbf{E} = \nabla\times(\mu\mathbf{H})$ where $\varepsilon = 1/\mu\mathfrak{c}^2$, and the speed of light $\mathfrak{c}$ is assumed to be much larger than the characteristic scale of the velocity field $\mathbf{u}$ (see [19,20] for more details).

To obtain a weak form of Ampère's theorem we proceed as in the electric scalar case. Choosing test functions $\mathbf{b}$ that satisfy the same boundary condition as $\mathbf{H}$ on Γ, we obtain

$$(\mu\partial_t\mathbf{H}, \mathbf{b})_\Omega + a_s(\mathbf{H},\mathbf{b}) + (\mathbf{E}, \nabla\times\mathbf{b})_{\Omega_v} = \left(\frac{1}{\sigma}\mathbf{j}, \nabla\times\mathbf{b}\right)_{\Omega_c}. \tag{16}$$

As for the electric scalar case, we can enforce weakly the constraint $\nabla\times\mathbf{H} = 0$ in Ω_v as follows

$$(\nabla\times\mathbf{H}, \mathbf{e})_{\Omega_v} = 0, \quad \forall \mathbf{e}. \tag{17}$$

It is at this very point that the 2D electric scalar situation differs from that of the 2D magnetic scalar and that of the full 3D case. In the 3D case, $\mathbf{E}$ is still the Lagrange multiplier for the constraint $\nabla\times\mathbf{H} = 0$ in Ω_v, but this multiplier must be chosen to satisfy the additional constraint $\nabla\cdot\varepsilon\mathbf{E} = 0$ in Ω_v. To account for this additional constraint on the Lagrange multiplier, we propose to enforce it in the least-squares sense by adding to the above equation the following bilinear form

$$d_s(\mathbf{e},\mathbf{e}') = (\nabla\cdot\varepsilon\mathbf{e}, \nabla\cdot\varepsilon\mathbf{e}')_{\Omega_v}. \tag{18}$$

Hence, we enforce $\nabla\times\mathbf{H}=0$ and $\nabla\cdot\varepsilon\mathbf{E}=0$ in Ω_v as follows:

$$(\nabla\times\mathbf{H},\mathbf{e})_{\Omega_v}-\delta_s d_s(\mathbf{E},\mathbf{e})=0,\quad \forall\mathbf{e}, \tag{19}$$

where δ_s is a positive free parameter yet to be fixed.

Finally, the weak formulation of (2) is as follows. For a given current $\mathbf{j}$ and an initial magnetic field $\mathbf{H}_0$ s.t. $\nabla\cdot(\mu\mathbf{H}_0)=0$,

$$\begin{cases}\text{Find } \mathbf{H} \text{ with } \mathbf{H}\times\mathbf{n}|_\Gamma=0 \text{ and } \mathbf{E} \text{ with } \mathbf{E}\cdot\mathbf{n}|_{\Gamma_v}=0 \text{ s.t.},\\ \mathbf{H}|_{t=0}=\mathbf{H}_0,\\ (\mu\partial_t\mathbf{H},\mathbf{b})_\Omega+a_s(\mathbf{H},\mathbf{b})+(\mathbf{E},\nabla\times\mathbf{b})_{\Omega_v}=\left(\dfrac{1}{\sigma}\mathbf{j},\nabla\times\mathbf{b}\right)_{\Omega_c},\quad \forall\mathbf{b} \text{ with } \mathbf{b}\times\mathbf{n}|_\Gamma=0,\\ (\nabla\times\mathbf{H},\mathbf{e})_{\Omega_v}-\delta_s d_s(\mathbf{E},\mathbf{e})=0,\quad \forall\mathbf{e} \text{ with } \mathbf{e}\cdot\mathbf{n}|_{\Gamma_v}=0.\end{cases} \tag{20}$$

2.2.2. Finite element discretization

Based on a finite element mesh $(\mathcal{T}_h)_{h>0}$, we introduce two finite element spaces of vector-valued function: $\mathbf{X}_h$ and $\mathbf{M}_h$. $\mathbf{X}_h$ is composed of continuous piecewise polynomials of degree two satisfying the boundary condition $\mathbf{b}_h\times\mathbf{n}|_\Gamma=0$, whereas $\mathbf{M}_h$ is composed of continuous piecewise polynomials of degree one satisfying the boundary condition $\mathbf{e}_h\cdot\mathbf{n}|_{\Gamma_v}=0$.

Denoting again by $\mathcal{I}_h$ the Lagrange interpolation operator and by d_t the finite difference temporal operator, we build an approximate solution to (20) as follows:

$$\begin{cases}\text{Find } \mathbf{H}_h\in\mathcal{C}^1(0,T;\mathbf{X}_h) \text{ and } \mathbf{E}_h\in\mathcal{C}^0(0,T;\mathbf{M}_h) \text{ s.t.},\\ (\mu d_t\mathbf{H}_h,\mathbf{b}_h)_\Omega+a_s(\mathbf{H}_h,\mathbf{b}_h)+(\mathbf{E}_h,\nabla\times\mathbf{b}_h)_{\Omega_v}=\left(\dfrac{1}{\sigma}\mathbf{j},\nabla\times\mathbf{b}_h\right)_{\Omega_c},\quad \forall\mathbf{b}_h\in\mathbf{X}_h,\\ (\nabla\times\mathbf{H}_h,\mathbf{e}_h)_{\Omega_v}-\delta_s d_s(\mathbf{E}_h,\mathbf{e}_h)=0,\quad \forall\mathbf{e}_h\in M_h,\\ \mathbf{H}_h|_{t=0}=\mathcal{I}_h\mathbf{H}_0.\end{cases} \tag{21}$$

The convergence analysis of this formulation, reported in [17], shows that the best convergence estimates are obtained if the free parameter δ_s is chosen to be equal to the mesh size, h. Hence, hereafter we choose $\delta_s=h$.

It is believed, though not yet proved completely, that the setting described above is such that an appropriate inf-sup condition like (14) holds in the 3D situation; we refer to [17] for the mathematical details.

3. Electric scalar cases

We study configurations with $E_z\neq0$ and $H_z=0$ in various geometries, where both the velocity and magnetic lines are planar. To assess the performance of the finite element algorithm described in Section 2.1.2, we first compare analytic solutions and numerical computations in the case of ohmic decay and in the case of a circular rotating conductor embedded in vacuum. Situations with no analytic solutions are also investigated such as a square conductor and a circular conductor embedded in conducting regions. Then we consider cases where the magnetic field lines are stretched by the flow, which is one of the basic physical mechanisms involved in dynamo action.

3.1. Ohmic decay

We consider a solid conducting circular cylinder of radius $R=1$ embedded in vacuum,

$$\Omega=\mathbb{R}^2,\qquad \Omega_c=\left\{(x,y)\in\mathbb{R}^2,\ \sqrt{x^2+y^2}<R\right\}. \tag{22}$$

A uniform magnetic field parallel to the x-axis is sustained in the whole domain for $t\leqslant0$ and is turned off for $t>0$. We study the evolution of the magnetic field for $t\geqslant0$.

3.1.1. Analytical computation

Let us briefly recall how the analytic solution to this problem can be found. It can be inferred from (2) that, in non-dimensional units, the magnetic field is a solution to the following set of equations,

$$\frac{\partial\mathbf{H}}{\partial t}=\Delta\mathbf{H}\quad \text{for } r\leqslant1,\quad \text{rot}\,(\mathbf{H})=0\quad \text{for } r>1,\quad \text{and}\quad \nabla\cdot\mathbf{H}=0\quad \text{in } \Omega, \tag{23}$$

with $\mathbf{H}$ continuous across Σ and $\|\mathbf{H}\|\to0$ for $r\to+\infty$. Using polar coordinates $(\mathbf{e}_r,\mathbf{e}_\varphi,\mathbf{e}_z)$, the magnetic field may be represented as

$$\mathbf{H}(r,\varphi,t)=\Re\left[\sum_m\left(b_r^m(r,t)\mathbf{e}_r+b_\varphi^m(r,t)\mathbf{e}_\varphi\right)\exp(\mathrm{i}m\varphi)\right], \tag{24}$$

Table 1

m	1	2	3	4
λ_m	5.783	14.682	26.375	40.706

Table 2

Case	λ_1	Error (%)	n_e	n_p	h
1	5.678	1.82	2320	1201	0.15
2	5.776	0.12	7670	3916	0.15

where m is the azimuthal wavenumber. $\mathbf{H}$ being solenoidal, we introduce the stream-function ψ such that $\nabla\times(\psi\mathbf{e}_z)=\mathbf{H}$, i.e.,

$$b_r^m = \mathrm{i}\frac{\psi_m}{r}, \qquad b_\varphi^m = -\frac{1}{m}\frac{\partial\psi_m}{\partial r}. \tag{25}$$

The continuity of $\mathbf{H}$ at $r=1$ forces the continuity of ψ_m and its derivative. After some calculations, the solution reads:

$$\text{for } r\leqslant 1 \quad \begin{cases} b_r^m(r,t) = \mathrm{i}\frac{C_m\sqrt{\lambda_m}}{2m}\big[J_{m+1}\big(\sqrt{\lambda_m}r\big)+J_{m-1}\big(\sqrt{\lambda_m}r\big)\big]\exp(-\lambda_m t), \\ b_\varphi^m(r,t) = \frac{C_m\sqrt{\lambda_m}}{2m}\big[J_{m+1}\big(\sqrt{\lambda_m}r\big)-J_{m-1}\big(\sqrt{\lambda_m}r\big)\big]\exp(-\lambda_m t), \end{cases} \tag{26}$$

$$\text{for } r>1 \quad \begin{cases} b_r^m(r,t) = \mathrm{i}C_m r^{-m-1}J_m\big(\sqrt{\lambda_m}\big)\exp(-\lambda_m t), \\ b_\varphi^m(r,t) = C_m r^{-m-1}J_m\big(\sqrt{\lambda_m}\big)\exp(-\lambda_m t), \end{cases} \tag{27}$$

where C_m is a constant, J_m are the Bessel functions of the first kind, and λ_m is determined by $J_{m-1}(\sqrt{\lambda_m})=0$. Table 1 gives some typical values of λ_m.

The smallest rate λ_1, corresponding to the decay time of the uniform initial magnetic field $m=1$, is numerically computed in the next section.

3.1.2. Numerical results

For numerical purposes the domain Ω is truncated. We consider the following two numerical domains,

$$\Omega_{1,h}=]-5R,+5R[^2 \quad \text{(case 1)}, \qquad \Omega_{2,h}=]-10R,+10R[^2 \quad \text{(case 2)}. \tag{28}$$

In each case we enforce $\mathbf{H}_h(t)\times\mathbf{n}$ to be zero at the boundary of the computational domain for $t>0$. To evaluate λ_1, we record the time evolution of the total magnetic energy,

$$\mathcal{E}(t)=\frac{1}{2}\int_\Omega \mu\mathbf{H}^2\,\mathrm{d}\mathbf{x}, \tag{29}$$

which decays as $\mathcal{E}(t=0)\exp(-2\lambda_1 t)$. A linear fit of the logarithm of $\mathcal{E}(t)$ gives λ_1, the decay rate. The numerical results obtained in the two cases are reported in Table 2. The three rightmost columns give, respectively, the number of finite elements n_e in each domain (i.e., the number of triangles used), the number of nodes n_p used for the computation of $\mathbf{H}_h$, and the typical mesh size h in the vicinity of the interface Σ. The number of elements to represent the conducting region is kept constant in the two simulations. We observe here that the larger the computational domain the more accurate the computation of λ_1.

3.2. Reconnections of magnetic field lines and steady regime in solid rotors

We again consider $\Omega=\mathbb{R}^2$, and a uniform magnetic field parallel to the x-axis, $\mathbf{H}_e=\mathbf{e}_x$, is applied in the whole domain at $t=0$ and at infinity for $t>0$. We study the evolution of the magnetic field and the stationary regime for simple rotor geometries embedded in insulating or conducting regions. The characteristic lengthscale and velocity are denoted as R and U respectively. Two timescales can then be constructed, the stretching time $\tau_s=R/U$ and the diffusive time $\tau_d=R^2\mu\sigma$.

3.2.1. Circular cylinder embedded in vacuum

We first consider a circular rotor of radius $R=1$

$$\Omega_c=\big\{(x,y)\in\mathbb{R}^2,\ \sqrt{x^2+y^2}<R\big\}. \tag{30}$$

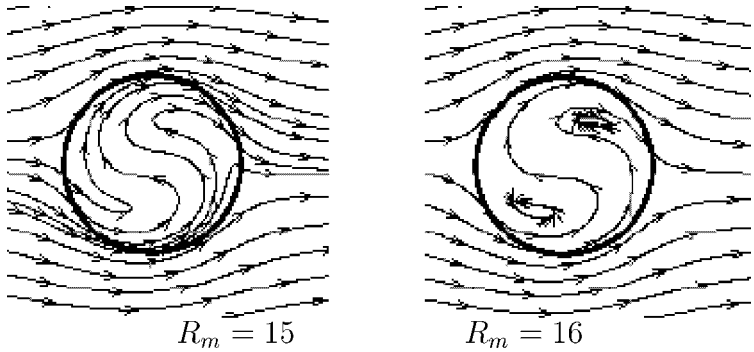

Fig. 2. Streamlines of the magnetic field. First observed reconnections at $\omega t = 4$. Rotation is counter-clockwise.[3]

At $t \leqslant 0$ the cylinder is at rest; at latter times it rotates with the velocity $\mathbf{u} = \omega \mathbf{e}_z \times \mathbf{r}$, where $\mathbf{r} = (x, y, 0)$ and $\mathbf{e}_z = (0, 0, 1)$. This problem has been studied first in [21] and analytic solutions have been derived. A distinctive feature of this problem is that the magnetic lines can reconnect to form closed loops during the transient regime.

The domain is truncated so that the actual computational domain is

$$\Omega_{1,h} =]-5R, +5R[^2, \tag{31}$$

whose numerical parameters are listed in the previous subsection: $n_e = 2320$, $n_p = 1201$, $h = 0.15$. At $t = 0$ we set $\mathbf{H}_0 = \mathbf{H}_e$ and for $t > 0$ we enforce $\mathbf{H} \times \mathbf{n}|_{\partial\Omega_{1,h}} = \mathbf{H}_e \times \mathbf{n}$. We perform simulations with different magnetic Reynolds numbers, $R_m = \mu\sigma\omega R^2$.

It is shown in [21] that no reconnection of the magnetic lines can occur if $R_m < R_m^c$, with $R_m^c \approx 15.46$, and, for magnetic Reynolds numbers slightly higher than R_m^c, one reconnection should occur at a time t such that $4 \leqslant \omega t \leqslant 5$. Numerically we observe no reconnection for $R_m = 15$, whereas one reconnection pair is observed for $R_m = 16$. These observations are compatible with the value of the critical magnetic Reynolds number obtained by Parker. We illustrate this phenomenon in Fig. 2 by showing the numerical magnetic lines at $\omega t = 4$ for the two cases $R_m = 15$ and $R_m = 16$.

In Fig. 3, we compare the analytic solution from [21] and the finite element one for $R_m = 100$. For times $\omega t = 1, 2, \ldots, 6$, the analytic solution is on the left of the figure and the numerical one is on the right. The first set of reconnections is observed in the time interval $2 \leqslant \omega t \leqslant 4$. Note that reconnections always occur in pairs.

As time goes to infinity, the solution reaches a steady state for which the magnetic lines cannot reconnect. We show some of these steady states in Fig. 4 for $R_m = 10$, 20, 40, and 100. We clearly observe in this figure the so-called skin effect: as the magnetic Reynolds number increases, the magnetic field is expelled from the conductor, and a boundary layer appears at the circumference of the cylinder. The skin width, or penetration length, is given by the formula $\delta = \sqrt{2\pi/\mu\sigma\omega} = R\sqrt{2\pi/R_m}$. For instance, at $R_m = 100$ we have $\delta/R = 0.25$. Note that this ratio is significantly larger than the grid size, $h = 0.15$, at the interface Σ; hence, the computation at $R_m = 100$ is meaningful. If the mesh size is too large with respect to δ/R, the computation remains numerically stable, but the precision deteriorates; for instance, the divergence of the magnetic field is no longer of the order of the consistency error.

In Fig. 5, the total magnetic energy for the magnetic Reynolds numbers $R_m = 10$, 20, 40, and 100 shows transient oscillations due to the successive reconnections. In the steady regime, the energy is a decreasing function of R_m and saturates at a level lower than the initial one due to expulsion of the magnetic field from the rotor. We clearly observe that the non-dimensional reconnection time scales like $\omega\tau_s = \omega R/U = 1$, while the non-dimensional time to reach steadiness scales like $\omega\tau_d = \omega R^2\mu\sigma = R_m$.

We observe that at steady state, the induced magnetic field $\mathbf{H}_{\text{ind}} = \mathbf{H} - \mathbf{H}_e$ outside the conductor is roughly that of a magnetic dipole whose angle with respect to the vertical axis varies with the magnetic Reynolds number (see [22]). For example, Fig. 6 shows the lines of the induced magnetic field at $R_m = 10$ and $R_m = 100$. The angles of the dipole, counted from the vertical axis, are 61° and 89° respectively, in accordance with [22]. Expulsion of the magnetic field from the rotor is achieved in the limit $R_m \to \infty$ as the angle of the dipole converges to 90°.

As R_m increases, the dipole axis rotates and tends to align itself with the opposite direction of the external field, and the intensity of the magnetic field inside the rotor approaches that of the external field. As a result, the magnetic energy in the rotor decreases to zero since it is contained in a shell of width comparable to the skin depth.

[3] The window size does not correspond to the computational domain in figures 2–4, 6, 10, 13, 19 in order to focus on the physical mechanism. In each case, or the radius is unity, or the size of the conducting square is 2. Each integration domain is defined in the text.

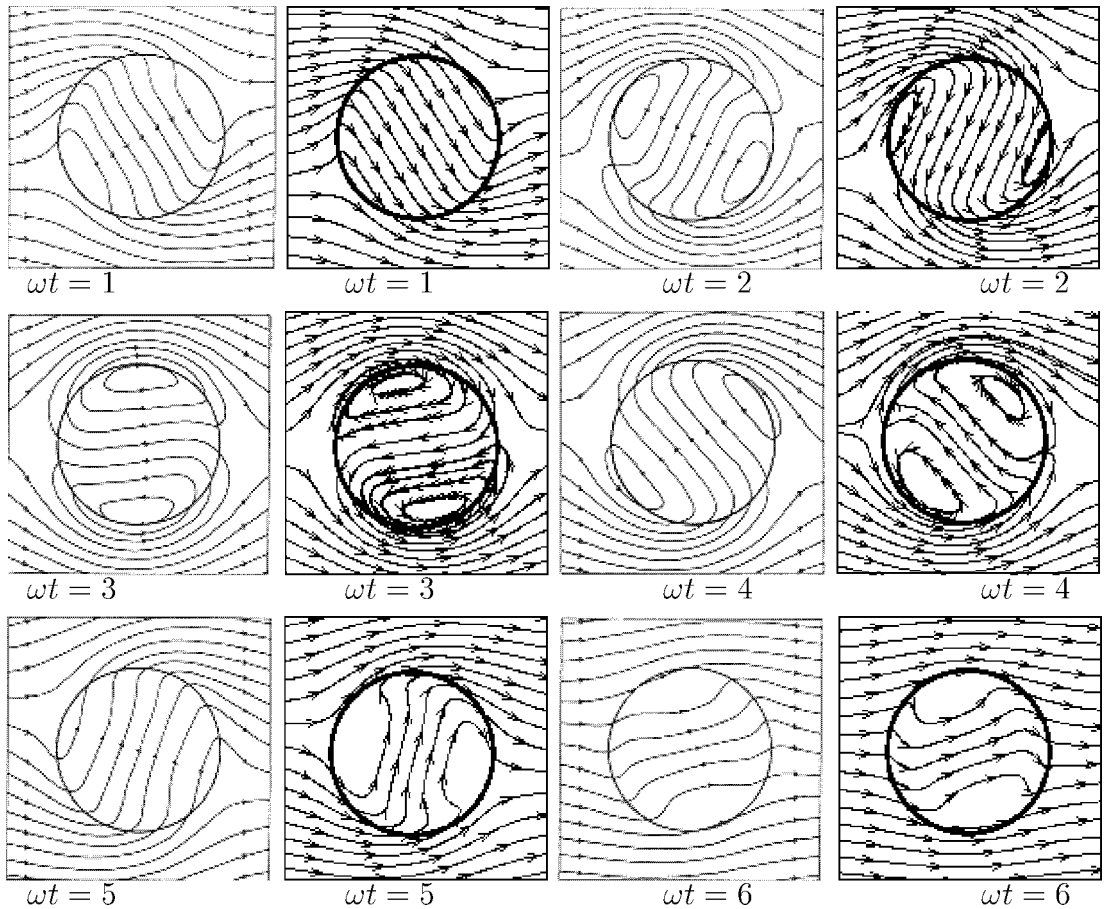

Fig. 3. Streamlines of the magnetic field, $R_m = 100$. Analytical solution from [21] (gray lines), our computations (dark lines). Rotation is clockwise.

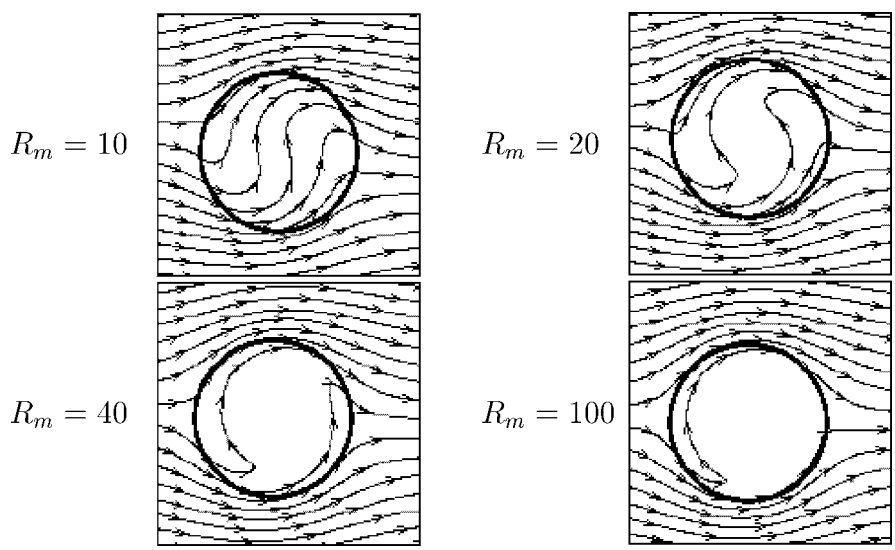

Fig. 4. Streamlines of the magnetic field at steady state. Rotation is counter-clockwise. Note the skin effect.

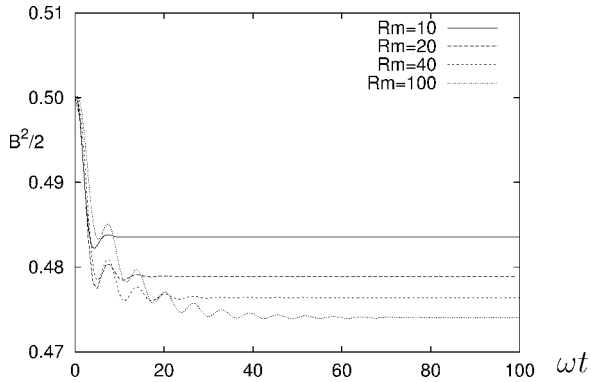

Fig. 5. Time evolution of the total magnetic energy for $R_m = 10, 20, 40, 100$ in non-dimensional time unit ωt for the rigid rotor in vacuum.

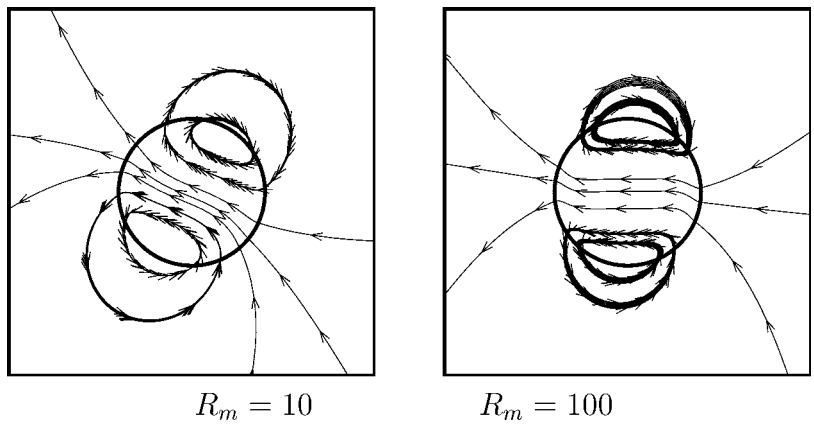

Fig. 6. Streamlines of the induced magnetic field $\mathbf{H}_{\text{ind}} = \mathbf{H} - \mathbf{H}_e$ showing a dipole structure at $R_m = 10$ and $R_m = 100$. Rotation is counter-clockwise and the imposed external fluid is $\mathbf{H}_e = \mathbf{e}_x$.

3.2.2. Square cylinder embedded in vacuum

Keeping the same boundary conditions and initial data as in the previous example, we now consider a rotating conducting cylinder of square section and of side $L = 2$,

$$\Omega_c = \left]-\frac{L}{2}, +\frac{L}{2}\right[^2. \tag{32}$$

There is no known analytic solution for this case. The interface between the insulating and the conducting media is time dependent. To avoid rebuilding the grid at each time step, we change the frame of reference so that the conducting cylinder is kept fixed in a uniform magnetic field rotating with the angular velocity ω.

The numerical simulations are performed by using the following truncated domain

$$\Omega_h = \left]-\frac{5L}{2}, +\frac{5L}{2}\right[^2, \tag{33}$$

at the boundary of which we enforce $\mathbf{H}_h(t) \times \mathbf{n} = (\cos(\omega t)\mathbf{e}_x + \sin(\omega t)\mathbf{e}_y) \times \mathbf{n}$ for $t > 0$. The Reynolds number is defined to be $R_m = \mu\sigma\omega(L/2)^2$.

The two main differences with the rotor of circular cross section are that, during the transient phase, the threshold for the first reconnections is lowered and more than two reconnections can occur at a given time.

The lowering of the critical magnetic Reynolds number is illustrated in Fig. 7. We show the magnetic lines at $\omega t = 2.7$ for $R_m = 8$ and $R_m = 9$. Our numerical simulations show that no reconnection occur for $R_m = 8$, whereas there is one pair for $R_m = 9$ at $\omega t = 2.7$; these results suggest $8 < R_m^c < 9$.

To illustrate the fact that, when Ω_c is a square, more than one pair of reconnections can occur at the same time, we show in Fig. 8 the magnetic lines at $\omega t = 11$ for $R_m = 20$. Four reconnections are clearly visible.

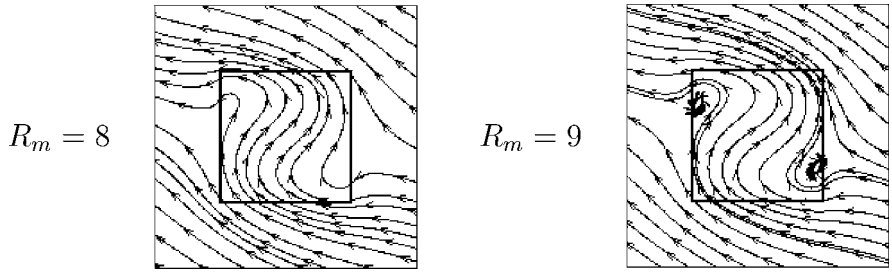

Fig. 7. Streamlines of the magnetic field. First observed reconnections at $\omega t = 2.7$.

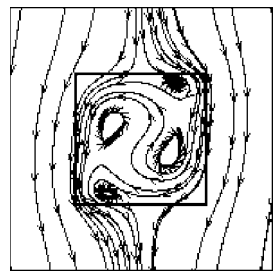

Fig. 8. Streamlines of the magnetic field. Two pairs of reconnections at $\omega t = 11$, $R_m = 20$.

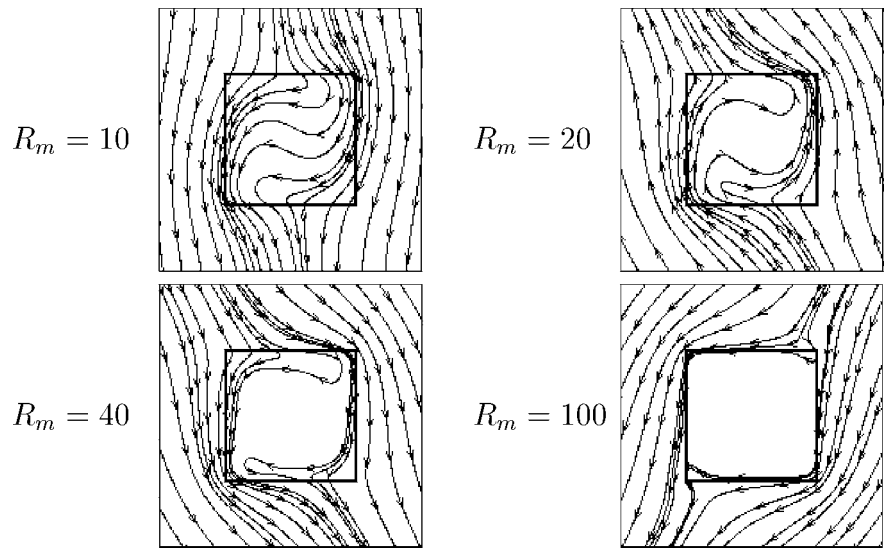

Fig. 9. Streamlines of the magnetic field at steady state. Note the skin effect.

As in the case of the circular cylinder, for a given R_m, reconnections cease when $t \to +\infty$, and the magnetic field is progressively expelled from the conducting medium as R_m increases. This skin effect is illustrated in Fig. 9 and qualitatively resembles that observed for the rotor of circular cross section shown in Fig. 4.

3.2.3. Circular cylinder embedded in a conducting region

To demonstrate the ability of the FEM code to cope with various kind of boundary conditions, we have surrounded the circular cylinder of radius $R = 1$ with a cylindrical conductive shell of radius a. Two cases are considered: a finite shell with the ratio $a/R = 1.5$ and an "infinite" shell with $a/R \to \infty$ (i.e., in this case the numerical domain is uniformly conductive). These two cases are compared with the reference situation corresponding to the ratio $a/R = 1$.

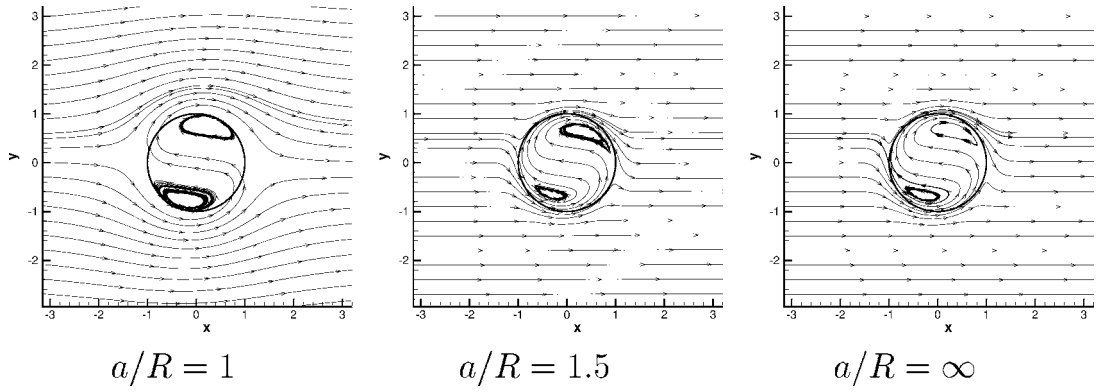

Fig. 10. Magnetic lines showing a pair of reconnections at $\omega t = 3$ for $R_m = 100$. Rotation is counter-clockwise.

The circular conducting region is then

$$\Omega_c = \big\{(x, y) \in \mathbb{R}^2,\ r = \sqrt{x^2 + y^2} < a\big\}, \tag{34}$$

and solid body rotation, $\mathbf{u} = \omega \mathbf{e}_z \times \mathbf{r}$, is imposed within $\{r \leqslant R = 1\}$, such that the velocity is discontinuous at $r = R$. For all ratios $a/R \geqslant 1$, the stationary solution coincides with the analytic steady state solution corresponding to $a/R = 1$ described in Section 3.2.1 as proved by [1], but the transient evolution for $a/R > 1$ can only be determined numerically.

The actual computational domain is

$$\Omega_{1,h} =]-5R, +5R[^2, \tag{35}$$

whose numerical parameters are: $n_e = 2320$, $n_p = 1201$, $h|_{r=R} = 0.15$. The numerical modeling of $a/R \to \infty$ is done by setting $\Omega_c = \Omega_{1,h}$, and we henceforth refer abusively to this situation by using the notation $a/R = \infty$.

The magnetic lines show similar reconnections in the three cases, and these reconnections are always located within the rotor. Fig. 10 shows the magnetic lines for $R_m = 100$ at the time $\omega t = 3$, which corresponds to the first maximum of the magnetic energy in the case $a/R = 1.5$.

The main qualitative difference we observe between the three cases considered is that, beyond $r/R \geqslant 2$, the magnetic lines are curved in the reference case $a/R = 1$, whereas they are straight and parallel to the imposed external field outside the rotor in the two other cases. Since, at short times ($\omega t = 3 \sim \omega\tau_s \ll \omega\tau_d$), the external induced field is restricted to a shell of width comparable to the skin depth δ, the external magnetic field beyond $r \geqslant R + \delta$ is very close to the imposed field $\mathbf{H}_e$. Significant differences are also observed when looking at the time evolution of the total magnetic energy (Fig. 11). Due to the intense stretching effects occurring at $r = R$, the amplitude of the oscillations induced by the reconnections increases significantly with a/R. At the time $\omega t = 120$, the energy for $a/R = 1.5$ differs from that for $a/R = 1$ by less than 0.1%, whereas the energy for $a/R = \infty$ decreases very slowly with time. The time for convergence to the common steady state is the diffusive timescale $\omega\tau_d(a/R) = \omega a^2 \mu\sigma = R_m (a/R)^2$. This time is $100 \times 5^2 = 2500$ in the case we denote by $a/R = \infty$, since in this case $a/R \approx 5$.

This example shows that enforcing inadequate artificial boundary conditions at $r = R$ to model the external non-conducting medium may have dramatic effects on the computed solution.

3.3. Stretching of magnetic field lines by eddies

Although 2D flows cannot lead to dynamo action, as is well known from anti-dynamo theorems [1], they nevertheless exhibit the main fundamental MHD processes, such as transient enhancement and final dissipation of magnetic fields by differential rotation (the so-called Ω effect), or amplification in a converging flow. Aside from a few analytic solutions of academic interest, the numerical approach is mandatory to have access to the time-dependent solution of the induction equation.

The goal of this section is to study the effects of simple fluid eddies on an external uniform magnetic field. The domain is $\Omega = \mathbb{R}^2$ and Ω_c is a circular cylinder of radius $R = 1$ containing a conducting fluid.

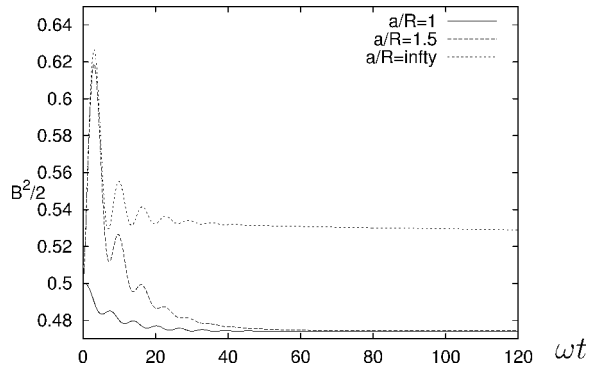

Fig. 11. Evolution of the total magnetic energy with respect to the non-dimensional time ωt for $R_m = 100$ and $a/R = 1,\ 1.5,\ \infty$.

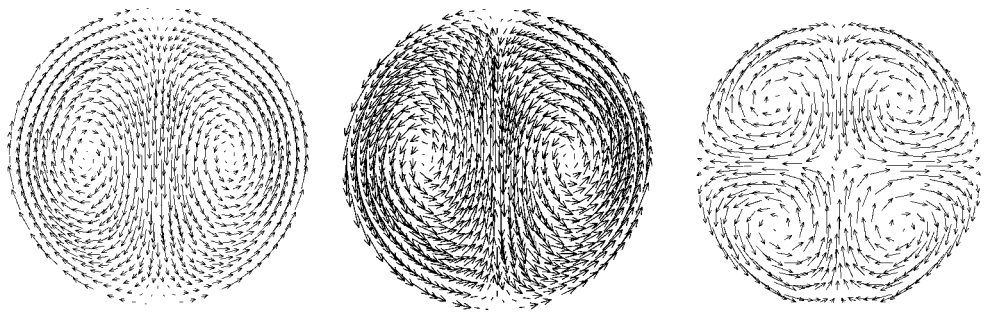

Fig. 12. Velocity vector fields for j_1^- (left), j_1^+ (middle), and j_2 (right).

3.3.1. The physical setting

To account for realistic flows, we henceforth choose velocity fields that are solutions to the 2D Euler equations. In polar coordinates, the velocity field assumes the following form:

$$\begin{cases} u_r = -\dfrac{m}{r} J_m(\lambda_m r)\sin(m\theta), \\ u_\theta = \lambda_m \dfrac{\partial J_m}{\partial r}(\lambda_m r)\cos(m\theta), \end{cases} \tag{36}$$

for $r \leqslant R = 1$ where J_m are the Bessel functions of the first kind and λ_m is the first real root of J_m. Denoting $U_{\max}$ the maximum flow speed, the magnetic Reynolds number is defined by $R_m = \sigma\mu U_{\max} R$ and time is given in units of turn-over time $\tau_s = R/U_{\max}$ for cases in Sections 3.3.2, 3.3.3, and 3.3.4.

We shall consider three cases: the first one, $m = 1$ and $\lambda_1 \approx 3.83171$, consists of two counter-rotating vortices (this field is hereafter referred to as the j_1^- velocity field); the second one consists of two co-rotating vortices obtained by using the j_1^--flow on the right half plane $x \geqslant 0$ and the j_1^--flow reflected through the origin on the left half plane $x < 0$ (it is hereafter referred to as the j_1^+ field); the third one, $m = 2$ and $\lambda_2 \approx 5.13562$, consists of four counter-rotating vortices creating a stagnation point at the center of the cylinder (it is hereafter referred to as the j_2 field). The three velocity fields are shown in Fig. 12.

The numerical simulations are performed in a truncated domain Ω_h which will be described in due time for each configuration. Two geometries for the imposed magnetic field are tested: $\mathbf{H}_e = \mathbf{e}_x$ and $\mathbf{H}_e = \mathbf{e}_y$. At $t = 0$ we set $\mathbf{H}_0 = \mathbf{H}_e$ and for $t > 0$ we enforce $\mathbf{H} \times \mathbf{n} = \mathbf{H}_e \times \mathbf{n}$ at the boundary of Ω_h.

We have also studied the velocity field (36) with $m = 0$ and $\lambda_0 \approx 2.40483$ (data not reported here), for which the orientation of the applied uniform magnetic field is irrelevant. The time evolution of the magnetic energy and the patterns formed by the magnetic lines are similar to those of a solid rotor surrounded by a conductive shell: the magnetic field is initially stretched by the differential rotation term $(\mathbf{H}\cdot\nabla)\mathbf{u}$, and the magnetic energy settles to a value lower than the initial one.

3.3.2. Counter-rotating vortices

We first study the interaction between a horizontal magnetic field $\mathbf{H}_e = \mathbf{e}_x$ and the pair of counter-rotating vortices j_1^-. The numerical simulations are performed in the following truncated domain

$$\Omega_{1,h} =]-5R, +5R[^2 \tag{37}$$

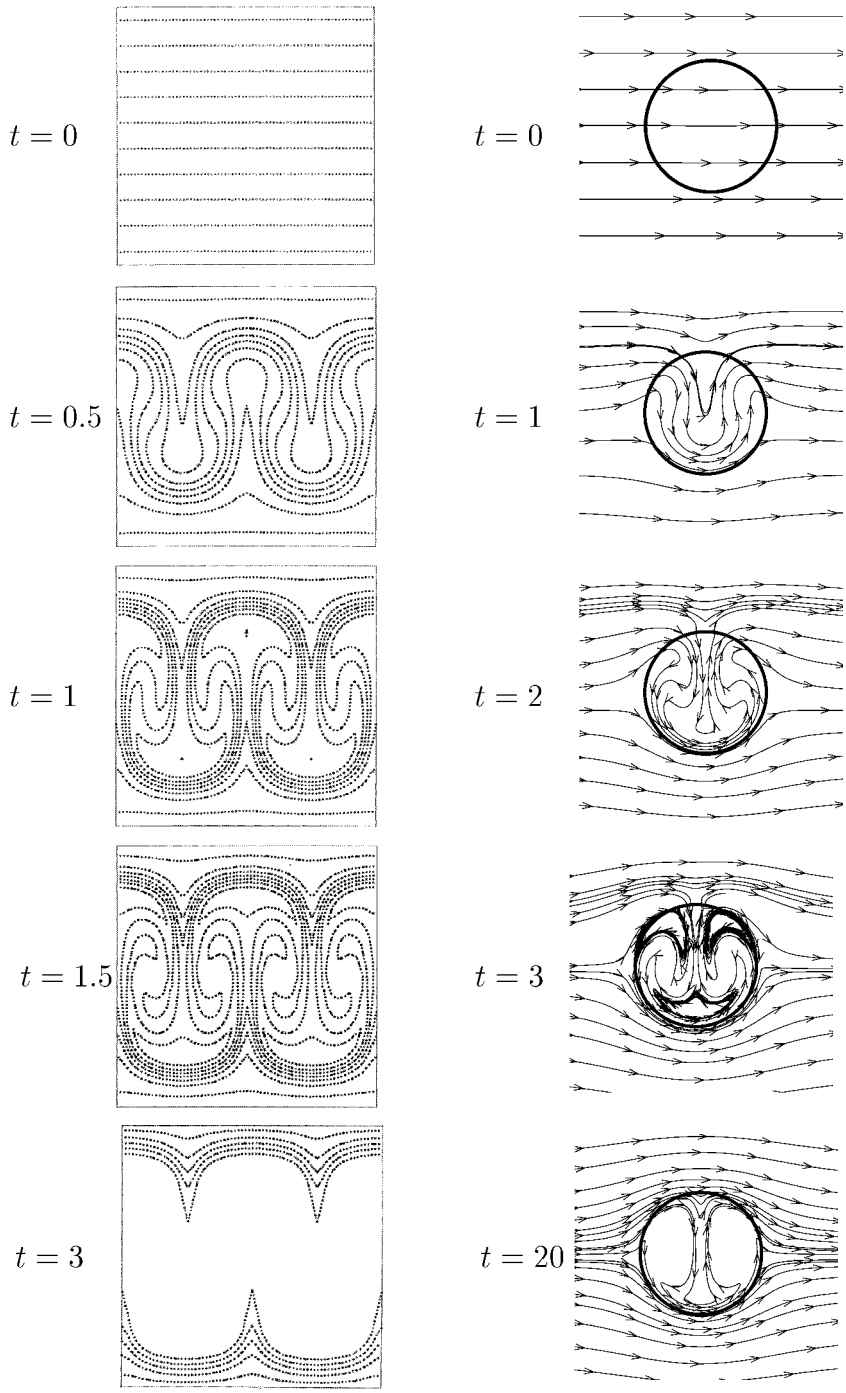

Fig. 13. Time evolution of the magnetic lines for counter-rotating vortices in turn-over time unit $U_{\max}t/R$; the imposed magnetic field is $\mathbf{H}_e = \mathbf{e}_x$. Left panels: Weiss' results; $R_m = 1000$; a single band of counter-rotating vortices; one conducting periodic slab. Right panels: our computations; $R_m = 100$; the j_1^- flow embedded in vacuum.

whose numerical parameters are: $n_e = 2320$, $n_p = 1201$, $h = 0.15$.

As time evolves, the applied uniform field is distorted by the velocity field and reconnections take place until a steady state is reached. A typical evolution of the magnetic lines is shown in the right panels of Fig. 13 for $R_m = 100$.

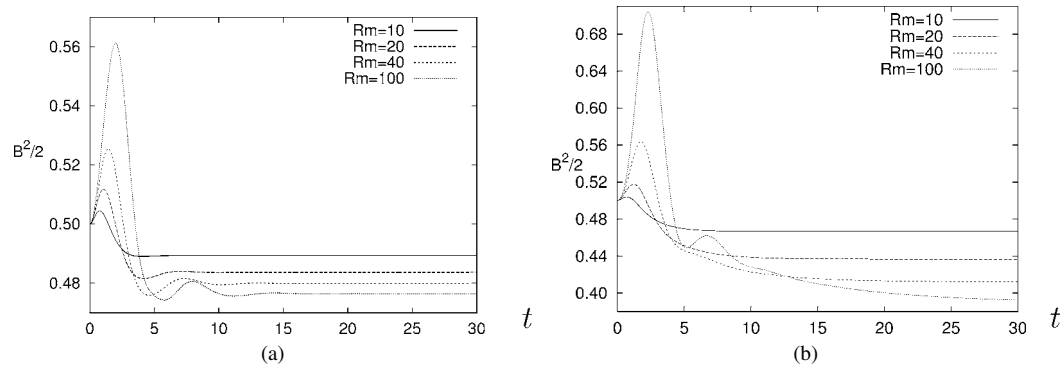

Fig. 14. Time evolution of the total magnetic energy in turn-over time unit $U_{\max}t/R$ for $R_m = 10$, 20, 40, 100 for the j_1^- case in vacuum subjected to (a) $\mathbf{H}_e = \mathbf{e}_x$, (b) $\mathbf{H}_e = \mathbf{e}_y$.

To make qualitative comparisons with our computations, we consider the results published in [23]. In this reference the conducting domain is $]-\frac{1}{2}, +\frac{1}{2}[^2$, boundary conditions are periodic at $x = \pm\frac{1}{2}$, and Dirichlet boundary conditions are enforced at $y = \pm\frac{1}{2}$, i.e., there is no insulating domain and the magnetic field lines are frozen at the top and bottom of the numerical box. The velocity field is defined by $\nabla \times (\psi \mathbf{e}_z)$ with the streamfunction $\psi = -\frac{1}{4\pi}(1 - 4y^2)^4 \sin(4\pi x)$. The results corresponding to these data (drawn from [23]) are shown on the left panels of Fig. 13 to be compared with our j_1^--solution. Note that the magnetic lines display similar patterns, although quantitative comparisons between our numerical results and Weiss' are out of question, for the geometries and the boundary conditions differ significantly.

The time evolution of the total magnetic energy is shown in Fig. 14(a). The energy amplification observed during the first rotation period is due to the stretching term $(\mathbf{H} \cdot \nabla)\mathbf{u}$ which induces reconnections of the magnetic lines in a way very similar to what is observed in the rigid rotor case (see Section 3.2.3). As time increases, the magnetic field finally settles to a steady state. The final energy is a decreasing function of R_m.

We have also studied the interaction of a vertical magnetic field $\mathbf{H}_e = \mathbf{e}_y$ with the j_1^- flow embedded in vacuum. The numerical simulations are performed in the following truncated domain

$$\Omega_{2,h} =]-2R, +2R[^2 \tag{38}$$

whose numerical parameters are: $n_e = 2610$, $n_p = 1332$, $h = 0.075$. The spatial resolution is refined in this case to ascertain accuracy. The time evolution of the total energy corresponding to this situation is presented in Fig. 14(b). We observe the same types of features as those obtained by applying the horizontal magnetic field.

However, when comparing the magnetic fields at steady state, we observe significant differences. For $\mathbf{H}_e = \mathbf{e}_x$ (Fig. 13), the magnetic lines exhibit cusp-like points, while, for $\mathbf{H}_e = \mathbf{e}_y$, the magnetic field settles to a relatively smoother steady state (see Fig. 15 for $R_m = 100$) with a significant amplification in the converging part of the flow (near $x = 0$, $y = 0.6$). In both cases, the magnetic field is expelled from the vicinity of the two elliptic points of the flow.

To gain more insight on the amplification of the magnetic field that we observe at steady state in the region around the point $x = 0$, $y = 0.6$, when $\mathbf{H}_e = \mathbf{e}_y$, we represent in Fig. 16 the H_y-component of the magnetic field along the line $y = 0.6$ for $R_m = 10$, 20, 40, 100. As the skin depth $\delta = R\sqrt{2\pi/R_m}$ is the relevant lengthscale, we plot both the unscaled profiles $H_y(x, y = 0.6)$ and the rescaled ones $H_y(x\sqrt{R_m}, y = 0.6)$. We observe that the maximum amplitude of the field does not scale like $\sqrt{R_m}$ as obtained by Weiss in a periodic flow. Between $R_m = 10$ and 100, this quantity shows no power law dependence with R_m but seems to saturate as the magnetic Reynolds number increases, as already noted in the rotor case (see Section 3.2.1). This should be confirmed by runs at higher R_m on finer grids.

3.3.3. Co-rotating vortices

In this section we study the interaction of the j_1^+-flow with the enforced magnetic field $\mathbf{H}_e = \mathbf{e}_y$. Let us recall that the j_1^+-flow is obtained by keeping the j_1^- flow in the half plane $x \geqslant 0$, and by completing it in the half plane $x < 0$ by reflection through the origin. The resulting vector field is solenoidal, and its tangential component along the $x = 0$ axis is discontinuous (see the middle panel in Fig. 12).

The stretching term is locally diverging, but the FEM weak formulation allows for a discontinuous velocity field. Since we want to compare the FEM solution with a case considered by Weiss [23], the conductivity is assumed to be equal to 1 everywhere; i.e., we set

$$\Omega_c = \Omega_{2,h} =]-2R, +2R[^2 \tag{39}$$

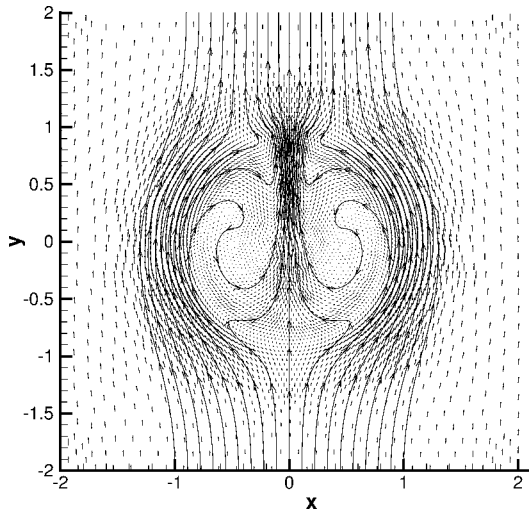

Fig. 15. Magnetic lines at steady state for the j_1^- case in vacuum, $R_m = 100$, and $\mathbf{H}_e = \mathbf{e}_y$.

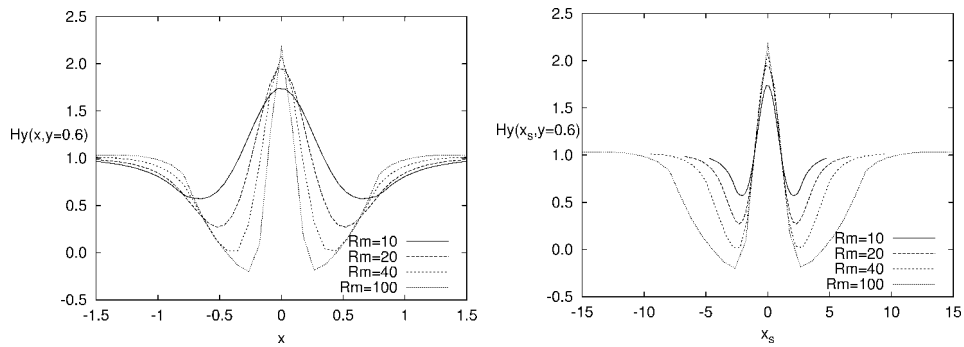

Fig. 16. Magnetic field profiles $H_y(x, y = 0.6)$ (a) and $H_y(x_s = x\sqrt{R_m}, y = 0.6)$ (b) for the j_1^--flow in vacuum and $\mathbf{H}_e = \mathbf{e}_y$.

(with $n_e = 936$, $n_p = 495$, $h = 0.15$). At $t = 0$ we set $\mathbf{H}_0 = \mathbf{H}_e$ and for $t > 0$ we enforce $\mathbf{H} \times \mathbf{n} = \mathbf{H}_e \times \mathbf{n}$ at the boundary of $\Omega_{2,h}$. The magnetic lines at steady state for $R_m = 100$ are shown in Fig. 17. We observe that magnetic lines cross the $x = 0$ axis which is compatible with the symmetry of the velocity field. Indeed, as $\mathbf{u}(x, y, t) = -\mathbf{u}(-x, -y, t)$ (central symmetry), then $\mathbf{H}(x, y, t) = +\mathbf{H}(-x, -y, t)$ with the appropriate boundary and initial conditions that we have used. Note that this crossing also occurs in the rotor case (see Section 3.2.1).

Weiss [23] has considered a similar case (referred to as "single eddy") with a velocity jump using a finite difference method and a spatially periodic flow. The flow is defined by the streamfunction $\psi = (-1/\pi)(1 - 4y^2)^4 \cos \pi x$. To keep clear of the divergence of the stretching term, the discontinuity of the velocity field is made to coincide with the periodic boundaries at $x = \pm 1/2$. The computational domain is fully conducting and Dirichlet conditions are imposed at the top and bottom of the numerical box, $y = \pm 1/2$. In contrast to our solution, the magnetic lines in Weiss' computation (see for example his Fig. 2) remain parallel to the vertical lines of discontinuity ($x = \pm 1/2$ corresponding to $x = 0$ in our case) and do not cross it. Once again, this example illustrates the fact that inadequate artificial boundary conditions may have important effects on the computed solution.

The time evolution of the magnetic energy for $R_m = 10, 40, 100$ is shown in Fig. 18. The results are similar to those obtained previously with the double vortex j_1^- flow.

3.3.4. Stagnation point

We finally consider the j_2-flow embedded in vacuum. This flow exhibits a stagnation point. This configuration is often studied in 3D for its ability to amplify the magnetic field. The numerical simulations are performed in the following truncated domain

$$\Omega_{1,h} =]-5R, +5R[^2 \tag{40}$$

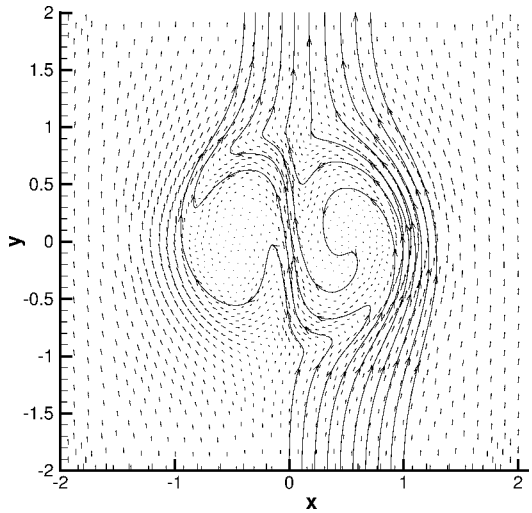

Fig. 17. Streamlines of the magnetic field at $R_m = 100$ in the steady state for the j_1^+ flow in a conducting domain and $\mathbf{H}_e = \mathbf{e}_y$.

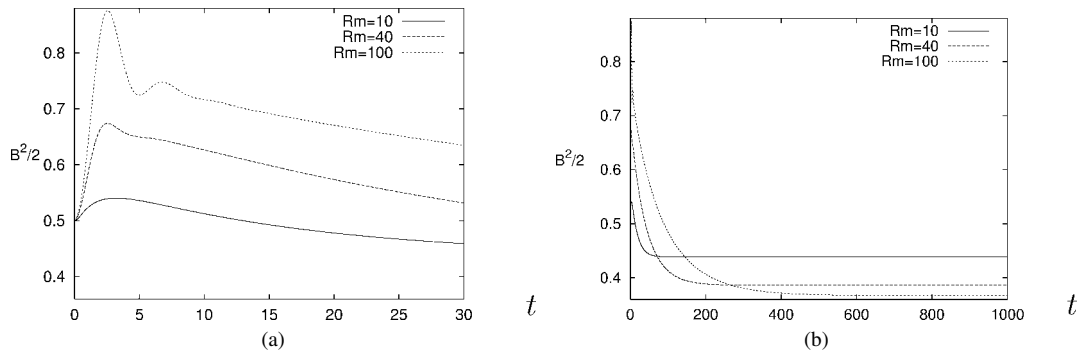

Fig. 18. Time evolution of the total magnetic energy in turn-over time unit $U_{\max} t/R$: (a) $0 \leqslant U_{\max} t/R \leqslant 30$; (b) until convergence; $R_m = 10$, 40, 100; j_1^+-flow in a conducting medium; $\mathbf{H}_e = \mathbf{e}_y$.

whose numerical parameters are: $n_e = 2320$, $n_p = 1201$, $h = 0.15$. We set $\mathbf{H}_e = \mathbf{e}_y$, $\mathbf{H}_0 = \mathbf{H}_e$ at $t = 0$, and for $t > 0$ we enforce $\mathbf{H} \times \mathbf{n} = \mathbf{H}_e \times \mathbf{n}$ at the boundary of $\Omega_{1,h}$. Our solution obtained with $R_m = 100$ is shown in Fig. 19 (bottom right panel). We compare the magnetic lines to that of [23] at $R_m = 1000$ where the flow is defined by the streamfunction $\psi = \frac{1}{4\pi} \sin 2\pi x \sin 4\pi y$ if $|y| \leqslant \frac{1}{4}$ and $\psi = 0$ otherwise. The flow is shown in the top panel in Fig. 19, and the magnetic lines are shown in the bottom left panel. In both cases, inspection of the magnetic lines shows that inside the conducting region the magnetic flux is expelled from the vicinity of the four elliptic points and concentrate within tubes of width comparable to the skin depth. Note that in contrast to the j_1^--configuration, the converging region whose axis is perpendicular to the external magnetic field is inefficient (see Fig. 13).

3.4. Scaling laws for the internal magnetic energy

For all the preceeding velocity flows, the total magnetic energy at steady state decreases with R_m. This is in contrast with Weiss' results which requires some discussion. Since the vortices of Weiss are periodic, the final concentration of the magnetic field in tubes of transverse size scaling like $1/\sqrt{R_m}$ enforces the magnetic field to scale like $\sqrt{R_m}$, which is verified by Weiss' solutions. In the present work, we have considered isolated vortices and have verified that the $1/\sqrt{R_m}$ skin depth scaling is valid. However, the magnetic flux concentrated in a tube with a minimal width comparable to the skin depth stems from a boundary strip which varies with R_m, so that the flux tube argument used for the periodic flow cannot be invoked in the case of isolated eddies.

The internal magnetic energy E_{mi} at steady state is a function of R_m which can be computed numerically. In the solid rotor case, we expect that E_{mi} scales like $1/\sqrt{R_m}$ since the maximal field saturates and is concentrated in a shell of width

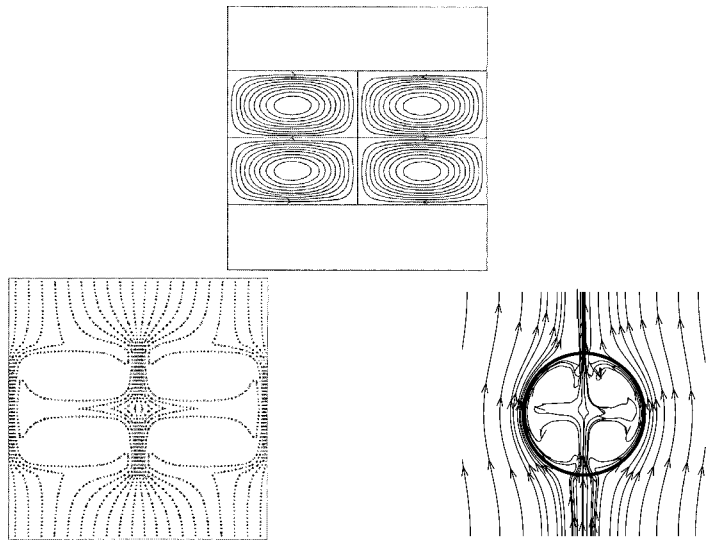

Fig. 19. Top: velocity lines for the double band of counter-rotating vortices considered by Weiss [23]. Bottom left: magnetic lines at steady state in the conducting periodic slab considered by Weiss, $R_m = 1000$. Bottom right: magnetic lines at steady state using the j_2-flow embedded in vacuum, $R_m = 100$. In both cases the imposed magnetic field is $\mathbf{H}_e = \mathbf{e}_y$.

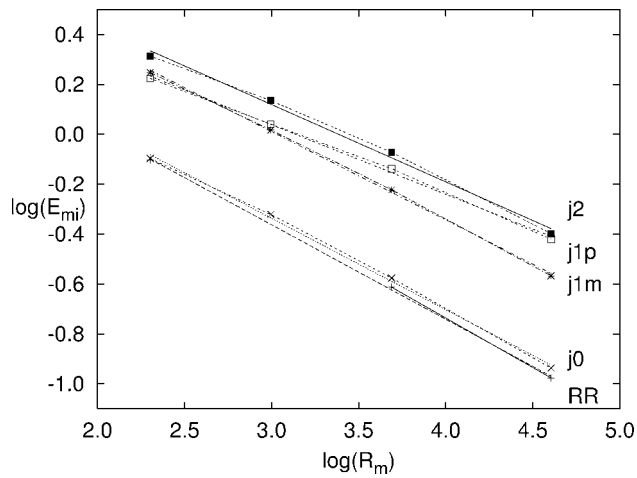

Fig. 20. Scaling laws $R_m^{-\beta}$ of the internal magnetic energy E_{mi} for different 2D flows as indicated: RR for rigid rotor, $\beta_{RR} = 0.38$; j0 for the j_0-flow, $\beta_{j_0} = 0.37$; j1m for the j_1^--flow, $\beta_{j_1^-} = 0.35$; j1p for the j_1^+-flow, $\beta_{j_1^+} = 0.28$ and j2 for the j_2-flow, $\beta_{j_2} = 0.31$.

comparable to the skin depth. Fig. 20 shows that E_{mi} scales like $R_m^{-\beta}$ for five different flows: solid rotor, j_0, j_1^+, j_1^- and j_2 for $10 \leqslant R_m \leqslant 100$. The slopes β vary between 0.28 and 0.38 for the truncated domain $\Omega_{1,h}$. The departure from $\beta_{\text{rotor}} = 0.5$ can be due to truncation discretization or to the narrow range of magnetic Reynolds numbers studied. In any case, the results suggest that E_{mi} is always a decreasing function of R_m for any 2D flow. This conjecture can be considered as a generalization of the anti-dynamo theorem for planar flows submitted to an external field.

This section shows that accounting properly for vacuum and enforcing proper boundary conditions is important in the context of the dynamo problem.

4. Magnetic scalar cases

We study configurations with $\mathbf{H} = H_z \mathbf{e}_z$ and $E_z = 0$ in various geometries, where both the velocity and the current field are planar. To assess the performance of the finite element algorithm described in Section 2.2.2, we first compare analytic solutions

and numerical computations for ohmic decay and induction heating. We next consider the generation of eddy currents with a magnetic Reynolds number of order unity. Finally we study the electric current flowing in a compound domain.

4.1. Ohmic decay

A constant magnetic field parallel to the z-axis is sustained in the whole domain, $\Omega = \mathbb{R}^2$, for $t \leqslant 0$ and is switched off at $t > 0$. Conducting media subjected to this type of condition develop Ohmic currents which control the decay of the magnetic field. To illustrate this effect, we consider the case of a conducting circular cylinder of radius $R = 1$ embedded in vacuum,

$$\Omega_c = \big\{(x, y) \in \mathbb{R}^2,\ \sqrt{x^2 + y^2} < 1\big\}. \tag{41}$$

The analytic solution to this problem can easily be calculated. Defining $\mathbf{H} = (0, 0, b)$, assuming axisymmetry, and recalling that the magnetic field is the solution to problem (23), we obtain

$$b(r, t) = \begin{cases} J_0\big(\sqrt{\lambda_0} r\big) \exp(-\lambda_0 t) & \text{for } r \leqslant 1, \\ 0 & \text{for } r \geqslant 1, \end{cases} \tag{42}$$

where $\sqrt{\lambda_0}$ is the first root of the Bessel function J_0, leading to $\lambda_0 \approx 5.783$.

The numerical simulations are performed in two truncated domains

$$\Omega_{0,h} =]-2R, +2R[^2 \quad \text{(case 1)}, \qquad \Omega_{1,h} =]-5R, +5R[^2 \quad \text{(case 2)}. \tag{43}$$

At $t = 0$ we set $\mathbf{H}_0 = \mathbf{e}_z$, and for $t > 0$ we set the magnetic field to zero at the external boundary, i.e., $\mathbf{H} \times \mathbf{n}|_{\partial\Omega_h} = 0$.

To evaluate the decay rate λ_0, we record the magnetic energy in time, $\mathcal{E}(t)$, then, assuming the decay $\mathcal{E}(t = 0) \exp(-2\lambda_0 t)$, we perform a linear fit of the logarithm of $\mathcal{E}(t)$. The results are reported in Table 3.

Table 3

Case	λ_0	Error (%)	n_e	n_p	h
1	5.882	1.72	424	239	0.3
2	5.812	0.50	2320	1201	0.15

As expected, the computed value of λ_0 in the second case is the closest to the analytic solution, since in this case the external boundary is farther from the interface Σ than in the first case, and the mesh is twice as fine. This conclusion is the same as that we have derived for Ohmic decay in the scalar electric case in Section 3.1.2.

4.2. Induction heating

It is well known that externally controlled time varying magnetic fields induce currents and Ohmic heating in conducting bodies. As an example of this phenomenon, we consider an harmonic magnetic field heating a circular cylinder of radius $R = 1$

$$\Omega = \mathbb{R}^2, \quad \text{and} \quad \Omega_c = \big\{(x, y) \in \mathbb{R}^2,\ \sqrt{x^2 + y^2} < 1\big\}. \tag{44}$$

Denoting by $H_e \exp(\mathrm{i}\omega t)$ the external magnetic field, setting $\mathbf{H} = (0, 0, b)$, and assuming the solution to be harmonic in time, the analytic solution to this problem is

$$b(r, t) = \begin{cases} H_e \dfrac{\mathrm{be}(r\sqrt{2\pi}/\delta)}{\mathrm{be}(\sqrt{2\pi}/\delta)} \exp(\mathrm{i}\omega t), & \text{for } r \leqslant 1, \\ H_e \exp(\mathrm{i}\omega t), & \text{otherwise}, \end{cases} \tag{45}$$

where $\delta = \sqrt{2\pi/\mu\sigma\omega}$ and $\mathrm{be}(r) \equiv \mathrm{ber}(r) + \mathrm{i}\,\mathrm{bei}(r) = J_0((-1 + \mathrm{i})r/\sqrt{2})$ is the Kelvin function (see [19] for more details).

The numerical simulation is performed on the truncated domain

$$\Omega_{0,h} =]-2R, +2R[^2. \tag{46}$$

The initial data is zero. The frequency of the external oscillating magnetic field is chosen to be $\omega = 2\pi$. For this frequency, the skin depth $\delta = 1$ is of the same order as $R = 1$, and one consequently expects only a moderate attenuation of the magnetic field within the conducting cylinder.

In Fig. 21, we have plotted the real amplitude of the numerical solution at $r = 1$, i.e., $b_{\mathrm{num}}(1, t)$, as a function of that at $r = 0$, i.e., $b_{\mathrm{num}}(0, t)$, for $0 \leqslant t \leqslant 2$. It is clear that the transient regime does not last more than one period.

Defining $\phi(r)$ to be the ratio of the complex amplitude of the magnetic field at radius r to that at radius $r = 0$ as $t \to +\infty$, our numerical solution gives $\phi_{\mathrm{num}}(1) \approx 1.51 \exp(\mathrm{i}\ 1.29)$. This function compares very well with the analytic one $\phi(1) = \mathrm{be}(\sqrt{2\pi}) \approx 1.52 \exp(\mathrm{i}\ 1.31)$.

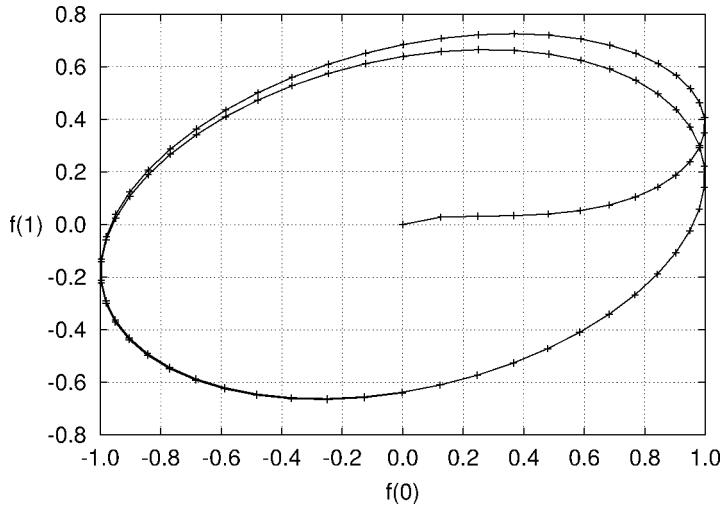

Fig. 21. Time evolution of the magnetic field at the conductor circumference as a function of the magnetic field at the centre. After $t > 1$, the forced steady regime is reached.

4.3. Eddy currents

Important industrial applications of magneto-dynamics consist of braking or driving bodies, either in solid or fluid state, by applying magnetic fields to conducting materials. In the present preliminary study, we illustrate the value of the FEM approach by showing a few academic 2D examples in this spirit.

An external static magnetic field is applied within a cross section only partially covering a moving conductor. Eddy currents are thus generated, and the corresponding Lorentz force acts against the movement. When the interface between the conducting and insulating media is close to the domain where the magnetic field is enforced, the eddy currents are influenced by edge effects, and in this case the numerical approach proves to be very convenient. Denoting by $\mathbf{H}_e$ the enforced external field and $\mathbf{h}$ the induced magnetic field, the total magnetic field is $\mathbf{H} = \mathbf{h} + \mathbf{H}_e$. This decomposition is inserted into the weak formulation (20) to obtain the evolution equation for $\mathbf{h}$. The external magnetic field is then accounted for as an external source current $\mathbf{j}_s = \mu\sigma(\mathbf{u} \times \mathbf{H}_e)$.

Let us consider a semi-infinite conducting plane, $\{x < 4\}$, moving with a rectilinear velocity, v, in the direction of the y-axis.

The truncated computational domain is the sum of the conductor,

$$\Omega_{c,h} = \big\{(x, y) \in \mathbb{R}^2,\ -4 \leqslant x < 4,\ -4 \leqslant y \leqslant 8\big\} \tag{47}$$

and of the vacuum,

$$\Omega_{v,h} = \big\{(x, y) \in \mathbb{R}^2, 4 \leqslant x \leqslant 12, -4 \leqslant y \leqslant 8\big\}. \tag{48}$$

The integration domain is shown on Fig. 22(a).

The external magnetic field, $\mathbf{H}_e$, is applied inside a circle of radius $R_1 = 1$ centred at $x_c = 1.5$, $y_c = 0$. It follows that in this area, there is an external source current, $\mathbf{j}_s = \mu\sigma(v\mathbf{e}_y \times \mathbf{H}_e)$. Since the eddy currents must flow freely from Γ_c, we enforce the following natural boundary conditions on Γ_c,

$$(\nabla \times \mathbf{h}) \times \mathbf{n}|_{\Gamma_c} = 0, \tag{49}$$

which, in the scalar magnetic case, amounts to $\partial_n h|_{\Gamma_c} = 0$.

Let us now give some details on how to enforce this boundary condition naturally. The PDE's we want to solve are

$$\begin{cases} \partial_t(\mu\mathbf{h}) = -\nabla \times \mathbf{E} & \text{in } \Omega, \\ \nabla \times \mathbf{h} = \sigma\big(\mathbf{E} + \mathbf{u} \times \big(\mu(\mathbf{h} + \mathbf{H}_e)\big)\big) & \text{in } \Omega_c, \\ \nabla \times \mathbf{h} = 0 & \text{in } \Omega_v, \\ \nabla \cdot \mathbf{E} = 0 & \text{in } \Omega_v, \\ \mathbf{h} \times \mathbf{n}|_{\Gamma_v} = 0, \quad (\nabla \times \mathbf{h}) \times \mathbf{n}|_{\Gamma_c} = 0, & \\ \mathbf{E} \cdot \mathbf{n}|_{\Gamma_v} = 0, & \\ \mathbf{h}|_{t=0} = \mathbf{h}_0. & \end{cases} \tag{50}$$

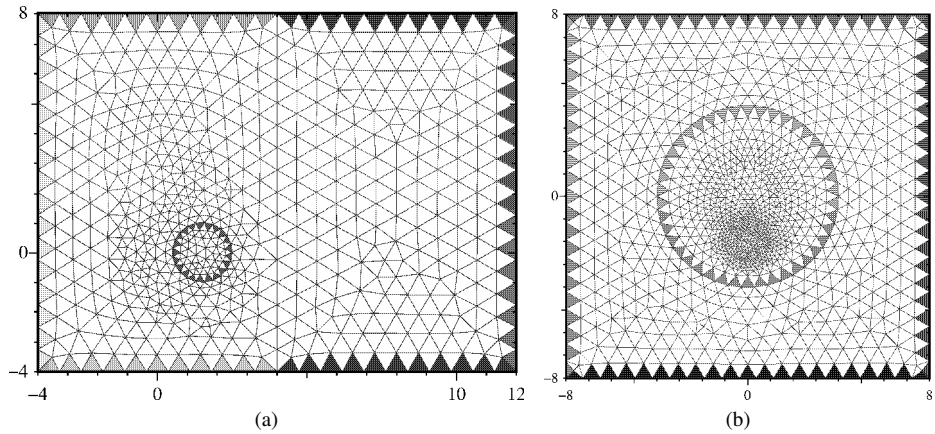

Fig. 22. Integration domains for the semi-infinite sheet (a) and disk case (b). The imposed magnetic field $\mathbf{H}_e$ is limited to an excentred disk of radius $R_1 = 1$ centred at (1.5; 0) for (a) and (0; −2) for (b).

Taking the scalar product of Faraday's law with a test function $\mathbf{b}$ and integrating by parts, we obtain

$$(\mu\partial_t\mathbf{h},\mathbf{b})_\Omega + \left(\frac{1}{\sigma}\nabla\times\mathbf{h},\nabla\times\mathbf{b}\right)_{\Omega_c} - (\mathbf{u}\times\mu\mathbf{h},\nabla\times\mathbf{b})_{\Omega_c} + (\mathbf{E},\nabla\times\mathbf{b})_{\Omega_v} + \int_\Gamma (\mathbf{E}\times\mathbf{n})\cdot\mathbf{b} = (\mathbf{u}\times\mu\mathbf{H}_e,\nabla\times\mathbf{b})_{\Omega_c}, \quad \forall\mathbf{b}. \tag{51}$$

By taking test functions that satisfy $\mathbf{b}\times\mathbf{n}|_{\Gamma_v} = 0$, and by using Ohm's law together with the fact that $\mathbf{H}_e|_{\Gamma_c} = 0$ (localization hypothesis) and $(\nabla\times\mathbf{h})\times\mathbf{n}|_{\Gamma_c} = 0$, the remaining surface integral reduces to

$$\int_\Gamma (\mathbf{E}\times\mathbf{n})\cdot\mathbf{b} = -\int_{\Gamma_c}\big((\mathbf{u}\times\mu\mathbf{h})\times\mathbf{n}\big)\cdot\mathbf{b}. \tag{52}$$

In conclusion, the weak equations to be solved are

$$\begin{cases} \big(\mu\partial_t\mathbf{h},\mathbf{b}\big)_\Omega + \left(\frac{1}{\sigma}\nabla\times\mathbf{h},\nabla\times\mathbf{b}\right)_{\Omega_c} - (\mathbf{u}\times\mu\mathbf{h},\nabla\times\mathbf{b})_{\Omega_c} + (\mathbf{E},\nabla\times\mathbf{b})_{\Omega_v} \\ \quad -\int_{\Gamma_c}\big((\mathbf{u}\times\mu\mathbf{h})\times\mathbf{n}\big)\cdot\mathbf{b} = (\mathbf{u}\times\mu\mathbf{H}_e,\nabla\times\mathbf{b})_{\Omega_c}, \quad \forall\mathbf{b}, \\ (\nabla\times\mathbf{h},\mathbf{e})_{\Omega_v} - \delta_s d_s(\mathbf{E},\mathbf{e}) = 0, \quad \forall\mathbf{e}, \\ \mathbf{h}|_{t=0} = \mathbf{h}_0, \quad \mathbf{E}\cdot\mathbf{n}|_{\Gamma_v} = 0, \quad \mathbf{h}\times\mathbf{n}|_{\Gamma_v} = 0. \end{cases} \tag{53}$$

It is the presence of the boundary integral in this weak formulation that enforces naturally the boundary condition $(\nabla\times\mathbf{h})\times\mathbf{n}|_{\Gamma_c} = 0$.

The contours of the induced magnetic field are represented in Fig. 23, where it can be seen that the larger the imposed velocity the longer the wake.

We have performed a parametric study of the Lorentz force as a function of the magnetic Reynolds number, $R_m = \mu\sigma v R_1$. The Lorentz force has a dominating braking component, F_y, while the horizontal component, F_x, is induced by the presence of the insulating medium. Fig. 24(a) shows the asymptotic value of F_y for $t\to+\infty$ as a function of R_m. It is clear from this figure that F_y is a linear function of R_m for $R_m \leqslant 0.1$. This linearity can be shown using the dynamo equation

$$\partial_t\mathbf{h} = R_m\nabla\times\big(\mathbf{u}\times(\mathbf{h}+\mathbf{H}_e)\big) + \nabla^2\mathbf{h} \tag{54}$$

scaled with the ohmic diffusion time $\tau_d = \mu\sigma R_1^2$. For $R_m \ll 1$, $|\mathbf{h}| \ll |\mathbf{H}_e|$, then $|\mathbf{h}|$ and $|\mathbf{j}|$ scale like $R_m|\mathbf{H}_e|$. The Lorentz force $F_y = -\mu j_x(h + H_e) \sim -\mu j_x H_e$ is then linear in R_m. At greater magnetic Reynolds numbers, the induced magnetic field cannot be neglected with respect to $|\mathbf{H}_e|$ and linearity in F_y is lost. Note that slow convergence toward the steady state is observed in the time evolution of F_x as shown in Fig. 24(b) for various R_m. This effect is the manifestation of the competition between induction and diffusion.

To be closer to real devices, we consider now a conducting circular cylinder of radius $R_2 = 4$ embedded in vacuum and rotating with the counter-clockwise angular velocity ω. The source is modelled by a constant magnetic field $\mathbf{H}_e$ parallel to the

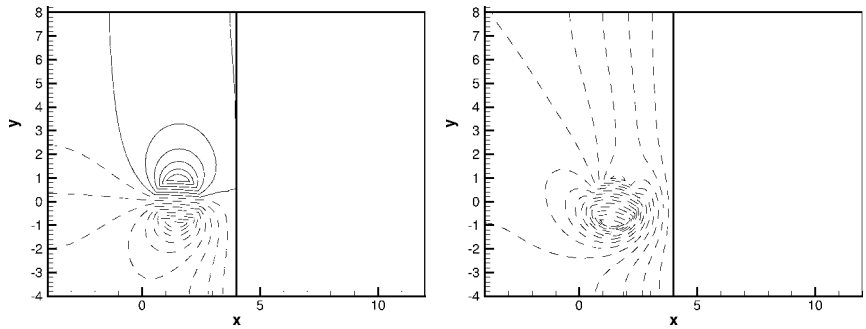

Fig. 23. Contours of the induced magnetic field in the half plane. $\mathbf{H}_e$ is limited to a disk of radius $R_1 = 1$ centred at $(1.5; 0)$. The thick solid line is the frontier between the conductor and the vacuum. Solid (dashed) lines correspond to positive (negative) values. The imposed velocity is (a) $v = 0.1$ and (b) $v = 1$.

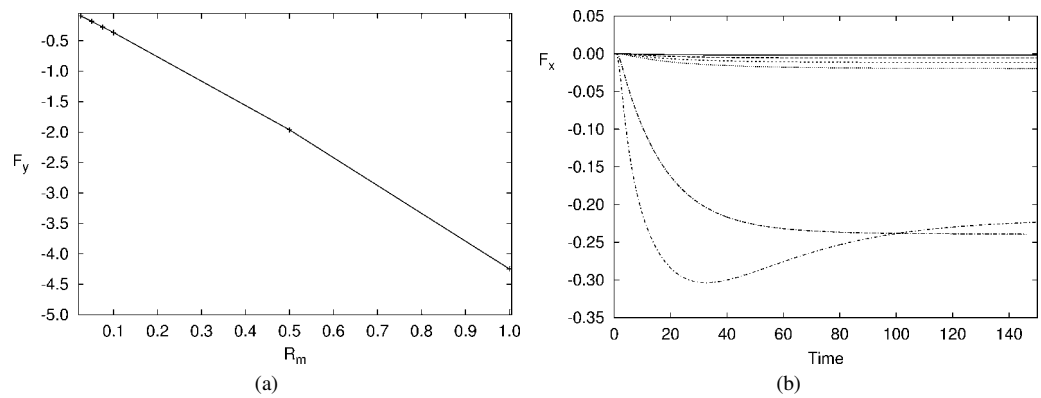

Fig. 24. Lorentz force: (a) F_y component as a function of R_m, (b) time evolution of F_x component as a function of R_m (from top to bottom at short times, $R_m = 0.025, 0.05, 0.075, 0.1, 0.5, 1.0$).

z-axis and applied within a disk of radius $R_1 = 1$ centred at $x_c = 0$, $y_c = -2$. The integration domain is shown in Fig. 22(b). Note that no natural boundary condition need be enforced since $\Gamma_c = \emptyset$.

The circulation of the eddy currents is limited to the circular region of radius R_2. For small magnetic Reynolds numbers, $R_m = \mu\sigma R_2^2\omega$, the contours of the induced magnetic field are approximately symmetric with respect to the vertical diameter as can be seen in Fig. 25(a) for $\omega = 0.1$ ($R_m = 1.6$). This distribution compares well with analytic results from [24] (not shown here).

At low magnetic Reynolds numbers, which is the case of practical applications, the induced field remains small compared to the applied field. If the latter is symmetric with respect to the meridian plane $x = 0$, see Fig. 25(a), then the induced field is antisymmetric, that is, $h_z(x, y, t) = -h_z(-x, y, t)$. At higher magnetic Reynolds numbers, the induced field becomes significant; therefore, the total magnetic field, which is the source term of the induced field (through the term $\sigma\mathbf{u} \times (\mathbf{h} + \mathbf{H}_e)$), is the sum of fields with different symmetry properties. This explains why the induced field represented in Fig. 25(b) has lost symmetry and has a wake-like shape instead.

4.4. Current flowing in a compound domain

In the preceding examples, the external magnetic field parallel to the z-axis was piecewise uniform and no imposed current was flowing. If the enforced external magnetic field has a constant gradient in a direction normal to Oz, then a uniform density current flows in the direction orthogonal to this gradient and orthogonal to Oz. We examine here the effect of an insulating obstacle on such a current.

To be more specific, a magnetic field parallel to the z-axis, of intensity -2 at $y = -4$ and $+2$ at $y = 4$, constant in time, is applied on a square domain of side $L = 8$,

$$\Omega =]-4, +4[^2. \tag{55}$$

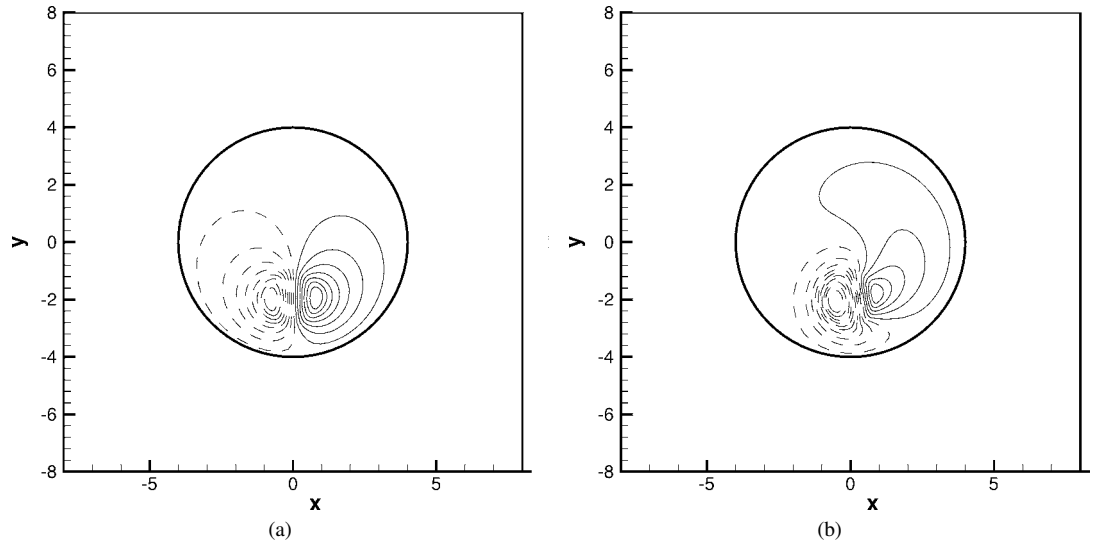

Fig. 25. Contours of the induced magnetic field in a domain consisting of a circular conductor of radius $R_2 = 4$ (thick solid line) embedded in vacuum. The imposed magnetic field $\mathbf{H}_e$ is limited to a disk of radius $R_1 = 1$ centred at $(0; -2)$. Solid (dashed) lines correspond to positive (negative) values. The imposed rotation rate is (a) $\omega = 0.1$ and (b) $\omega = 1$. Rotation is counter-clockwise.

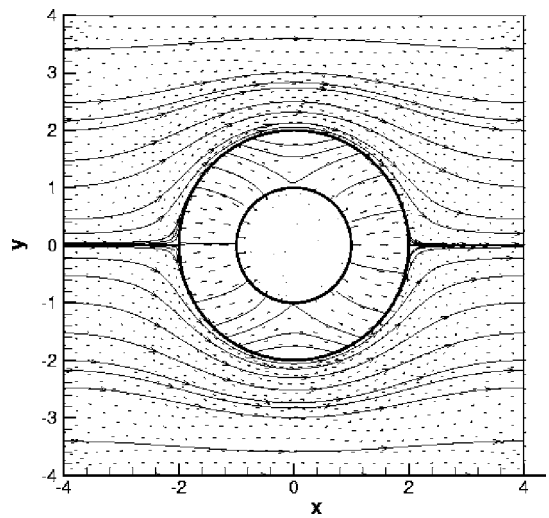

Fig. 26. Streamlines of the electric field in a domain composed by a circular conductor of radius $R_1 = 1$ embedded in vacuum of $R_2 = 4$ limited by a conducting square of side $L = 8$. Note the discontinuity of the normal component of the electric field at the interfaces.

Homogeneous Neumann conditions are enforced on the external vertical sides $x = \pm 4$. This boundary condition implies that a current intensity $+4$ is flowing in the x-direction through the section (y, z) of the domain. To demonstrate the ability of the FEM code to cope with successive matching conditions, a circular cylinder of radius $R_2 = 2$ centered at $(0, 0)$ forms an insulating obstacle to this current, and a conducting circular cylinder of radius $R_1 = 1$ is set in the middle of the insulating region. The streamlines of the steady electric field simulated numerically are shown in Fig. 26.

Due to the presence of the non-conducting cavity, the current streamlines are deviated. Surface charges appear at the boundary-vacuum interface, at $r = R_2 = 2$, such that the tangential component of electric field is continuous but its normal component is discontinuous. The presence of a conducting material without current at the centre forces the electric field to be zero in this region, i.e., for $r \leqslant R_1 = 1$. Continuity of the tangential component of the electric field across the interface $r = R_1 = 1$ forces the electric field to be normal there. The discontinuities of the normal component of the electric field are clearly apparent in Fig. 26.

5. Conclusion

We acknowledge the support of the ASCI laboratory (CNRS) where this work was initiated. We have tested numerically a new finite element technique for solving the Maxwell equations in the MHD limit in presence of conducting and non-conducting media. Contrary to penalization techniques (see [15]), we have accounted exactly for the insulating medium.

The limitation of our codes is that the boundary conditions at infinity are imposed at finite distance as in many other numerical studies. For practical purposes, we have seen that by using a sufficiently large integration domain, truncation errors can be reduced significantly (less than $\frac{1}{2}\%$ for an integration domain five times larger than the conductor).

We have preferred Lagrange finite elements to edge elements (the so-called Whitney elements) for their simplicity and, since Lagrange finite elements are natural candidates for solving the Navier–Stokes equations, we have preferred to restrict ourselves to these elements. We are aware that this choice may be restrictive in some circumstances. For instance, if simultaneously the conductor/insulator interface is not smooth and if μ is discontinuous then it may happen that the Lagrange finite element solution does not converge to the exact solution of the problem (see [25]). However, we do not expect this situation to occur in the dynamo context.

We have studied two families of 2D problems, where either the magnetic field or the current field is coplanar with the flow with magnetic Reynolds numbers up to 100. We have successfully compared our numerical results with some analytic solutions. We have also investigated physically relevant problems such as magnetic flux expulsion, magnetic field stretching, and eddy current generation. In each case, we have demonstrated the ability of the FEM formulation to compute physically consistent electric and magnetic fields in realistic domains.

The investigation of 3D cases using the algorithm described in [17] is currently in progress with a particular focus on the nonlinear dynamo action.

Acknowledgements

The authors have benefited from stimulating discussions with F. Rapetti and A. Bossavit. JLG gratefully acknowledges CNRS and the support of the Texas Institute for Computational and Applied Mathematics under TICAM Visiting Faculty Fellowships. CN acknowledges Philippe Meliga, of Ecole Polytechnique, for the results of Section 3.3 and Julien Messner, of Supaéro for the results of Section 3.2.1. Computations were performed at CINES (Centre Informatique National de l'Enseignement Supérieur).

References

[1] H.K. Moffatt, Magnetic Field Generation in Electrically Conducting Fluids, in: Cambridge Monographs Mech. Appl. Math., Cambridge University Press, Cambridge, 1978.
[2] T. Amari, J.F. Luciani, P. Joly, A preconditioned semi-implicit method for magnetohydrodynamics equation, SIAM J. Sci. Comput. 21 (1999) 970–986.
[3] N. Ben Salah, A. Soulaimani, W.G. Habashi, A finite element method for magnetohydrodynamics, Comput. Methods Appl. Mech. Engrg. 190 (43–44) (2001) 5867–5892.
[4] J.-F. Gerbeau, A stabilized finite element method for the incompressible magnetohydrodynamic equations, Numer. Math. 87 (1) (2000) 83–111.
[5] A.J. Meir, P.G. Schmidt, Analysis and numerical approximation of a stationary MHD flow problem with non-ideal boundary, SIAM J. Numer. Anal. 36 (1999) 1304–1332.
[6] M.L. Dudley, R.W. James, Time-dependent kinematic dynamos with stationary flows, Proc. Roy. Soc. London Ser. A 425 (1989) 407–429.
[7] J. Léorat, Numerical simulations of cylindrical dynamos: scope and method, in: 7th Beer-Sheva Onternatal Seminar, in: AIAA Progress in Astronautics and Aeronautic, Vol. 162, 1994, pp. 282–292.
[8] J. Léorat, Linear dynamo simulations with time dependent helical flows, Magnetohydrodynamics 31 (1995) 367–373.
[9] A. Gailitis, O. Lielausis, S. Dement'ev, E. Platacis, A. Cifersons, G. Gerbeth, T. Gundrum, F. Stefani, A. Christen, H. Hänel, G. Will, Detection of a flow induced magnetic field eigenmode in the Riga dynamo facility, Phys. Rev. Lett. 84 (2000) 4365–4368.
[10] R. Stieglitz, U. Muller, Experimental demonstration of a homogeneous two-scale dynamo, Phys. Fluids 13 (2001) 561.
[11] F. Stefani, G. Gerbeth, A. Gailitis, Velocity profile optimization for the Riga dynamo experiment, in: A. Alemany, Ph. Marty, J.P. Thibault (Eds.), Transfer Phenomena in Magnetohydrodynamics and Electroconducting Flows, Kluwer Academic, Dordrecht, 1999.
[12] A. Tilgner, A kinematic dynamo with a small scale velocity field, Phys. Lett. A 226 (1998) 75–79.
[13] M. Bourgoin, L. Marié, F. Pétrélis, C. Gasquet, A. Guigon, J.B. Luciani, M. Moulin, F. Namer, J. Burguete, A. Chiffaudel, F. Daviaud, S. Fauve, P. Odier, J.F. Pinton, Magnetohydrodynamics measurements in the von Kármán sodium experiment, Phys. Fluids 14 (2002) 3046–3058.
[14] J. Burguete, L. Marié, F. Daviaud, J. Léorat, Numerical study of homogeneous dynamo based on experimental von Kármán type flows, 2002, submitted for publication.

[15] J.Z.K.H. Chan, K. Zhang, G. Schubert, A non-linear, 3-D spherical α^2 dynamo using a finite element method, Phys. Earth and Planetary Interiors 128 (2001) 35–50.
[16] J.-L. Guermond, P.D. Minev, Mixed finite element approximation of an MHD problem involving conducting and insulating regions: the 2D case, Model. Math. Anal. Numer. 36 (3) (2002) 517–536.
[17] J.-L. Guermond, P.D. Minev, Mixed finite element approximation of an MHD problem involving conducting and Insulating regions: the 3D case, Numer. Methods Partial Differential Equations (2002), submitted for publication.
[18] N. Ben Salah, A. Soulaimani, W.G. Habashi, M. Fortin, A conservative stabilized finite element method for magnetohydrodynamics equations, Int. J. Numer. Methods Fluids 29 (1999) 535–554.
[19] A. Bossavit, Electromagnétisme en vue de la modélisation, in: Math. Appl., Vol. 14, SMAI/Springer-Verlag, Paris, 1993;
See also: Computational Electromagnetism, Variational Formulations, Complementary, Edge Elements, Academic Press, 1998.
[20] A. Bossavit, Computational Electromagnetism, Variational Formulations, Complementary, Edge Elements, in: Electromagnetism, Vol. 2, Academic Press, 1998.
[21] R.L. Parker, Reconnexion of lines of force in rotating spheres and cylinders, Proc. Roy. Soc. 291 (1424) (1966) 60–72.
[22] E.C. Bullard, Electromagnetic induction in a rotating sphere, Proc. Roy. Soc. A 199 (1949) 413–443.
[23] N.O. Weiss, The expulsion of magnetic flux by eddies, Proc. Roy. Soc. (1966).
[24] W.R. Smythe, Static and Dynamic Electricity, Hemisp. Pub. Corp., 1939.
[25] M. Costabel, A coercive bilinear form for Maxwell's equations, J. Math. Anal. Appl. 157 (2) (1991) 527–541.